NUMERICAL WAVE OPTICS INVESTIGATION OF OPTICAL SCATTER FROM STATISTICALLY ROUGH SURFACES

THESIS

Ann M. Lanari, Captain, USAF

AFIT-ENP-MS-17-M-099

DEPARTMENT OF THE AIR FORCE
AIR UNIVERSITY

AIR FORCE INSTITUTE OF TECHNOLOGY

Wright-Patterson Air Force Base, Ohio

AFIT-ENP-MS-17-M-099

NUMERICAL WAVE OPTICS INVESTIGATION OF OPTICAL SCATTER FROM STATISTICALLY ROUGH SURFACES

THESIS

Presented to the Faculty

Department of Engineering Physics

Graduate School of Engineering and Management

Air Force Institute of Technology

Air University

Air Education and Training Command

in Partial Fulfillment of the Requirements for the

Degree of Master of Science in Applied Physics

Ann M. Lanari, B.S.

Captain, USAF

March 2, 2017

AFIT-ENP-MS-17-M-099

NUMERICAL WAVE OPTICS INVESTIGATION OF OPTICAL SCATTER FROM STATISTICALLY ROUGH SURFACES

Ann M. Lanari, B.S.
Captain, USAF

Committee Membership:

Maj. Samuel D. Butler, PhD
Chair

Mark F. Spencer, PhD
Member

Michael A. Marciniak, PhD
Member

AFIT-ENP-MS-17-M-099

Abstract

The Bidirectional Reflectance Distribution Function (BRDF) describes optical scatter from surfaces by relating the incident irradiance to the exiting radiance over the entire hemisphere. Laboratory verification of BRDF models and experimentally populated BRDF databases are hampered by sparsity of monochromatic sources and ability to statistically control the surface features. Numerical methods are able to control surface features, have wavelength agility, and via Fourier methods of wave propagation, may be used to fill the knowledge gap. Monte-Carlo techniques, adapted from turbulence simulations, generate Gaussian distributed and correlated surfaces with an area of $1\,cm^2$, RMS surface height of $2.5\,\mu m$, and correlation length of $100\,\mu m$. The surface is centered inside a Kirchhoff absorbing boundary with an area of $16\,cm^2$ to prevent wrap around aliasing in the far field. These surfaces are uniformly illuminated at normal incidence with a unit amplitude plane-wave varying in wavelength from $3\mu m$ to $5\,\mu m$. The resultant scatter is propagated to a detector in the far field utilizing multi-step Fresnel Convolution and observed at angles from $-2\,\mu rad$ to $2\,\mu rad$. The far field scatter is compared to both a physical wave optics BRDF model (Modified Beckmann Kirchhoff) and two microfacet BRDF Models (Priest, and Cook-Torrance). Modified Beckmann Kirchhoff, which accounts for diffraction, is consistent with simulated scatter for multiple wavelengths for RMS surface heights greater than $\lambda/2$. The microfacet models, which assume geometric optics, are less consistent across wavelengths. Both model types over predict far field scatter width for RMS surface heights less than $\lambda/2$.

Acknowledgments

I would like to thank my committee, Maj Butler and Drs. Spencer and Marciniak for their thorough and thoughtful guidance throughout an unusual advising scenario. I would be remiss without acknowledging the tremendous help of Dr. Santasri Basu and Dr. Jack McCrae. Without their thorough explanations of various Fourier Techniques no simulation would have ever compiled. No amount of chocolate or homebaked goods will ever show my gratitude for their assistance to the strange student who just kept showing up in their offices.

To my classmates, whose commiseration and laughter brought great levity and camaraderie to the exacting circumstances of graduate school.

To my dear husband, who picked up so much slack at home, checked my math and my code, fixed my computer, lifted my spirits when I was frustrated, helped celebrate my victories however small, and made countless cups of tea, I'm filled with gratitude. And of course to my children, who cannot read, or do mathematics, but colored, or played alone through many eternities of waiting for mama to finish homework, you are more loved than you'll ever know.

Ann M. Lanari

Table of Contents

Page

List of Figures

Figure Page

List of Tables

NUMERICAL WAVE OPTICS INVESTIGATION OF OPTICAL SCATTER FROM STATISTICALLY ROUGH SURFACES

I. Introduction

1.1 Motivation

Remote sensing is utilized by the Air Force to capture information so that decisions can be made. In the case of hyperspectral remote sensing (HSRS) an image of the reflected and emitted power is taken by an imaging system, and a spectrometer captures the spectral content of the scene. The image shows the spatial distribution of light in the scene, while the spectral content measures the variation in power with respect to the wavelength of the reflected and emitted light. These sensors generally do not directly measure the desired information, but provide data from which the information may be extracted. In order to extract information, assumptions about the observables must be made [1]. In the case of identifying materials in a remote sensing scene, assumptions about how materials scatter light must be made.

For a perfectly smooth surface, the power would be reflected at an angle that mirrors the incident light as shown in Figure 1.1a; this is a specular response. A small intuitive leap would allow one to imagine a surface so rough that the light would be scattered in all directions uniformly, as shown in Figure 1.1b; this is a Lambertian response. In practice, neither of these surfaces exists, and the response is somewhere between the two ideal scenarios, there exists a specular response but also a significant non-specular response, as shown in Figure 1.1c. To describe the more general case, a Bidirectional Reflectance Distribution Function (BRDF) may be used.

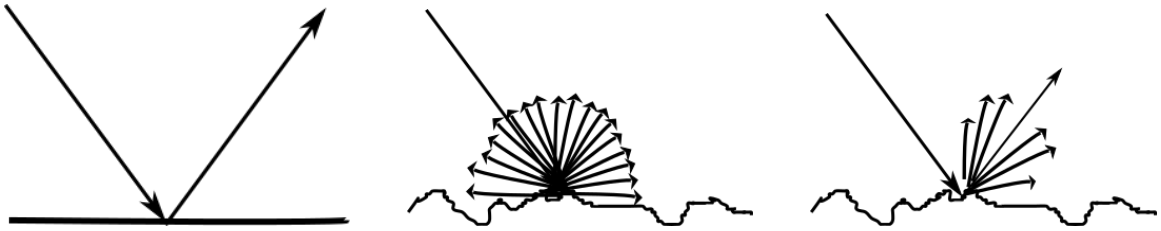

(a) Optically flat surface: all energy is reflected in the specular direction.

(b) Lambertian surfaces: energy is reflected in all directions equally.

(c) Realistic surface: reflected energy exhibits specular and non-specular responses.

Figure 1.1. Reflection from an ideal optical flat surface, an ideal Lambertian surface, and realistic surfaces

The BRDF is a 5-dimensional function that describes the angular dependence of the reflected light based on the angle of the incident light and its wavelength [2]. While this is a tidy solution, both electromagnetic calculations and physical measurements over the 5-dimensional space are almost intractably complex [3]. Although the BRDF literature is rife with models, the models which are computationally tractable for an HSRS system rely on geometric or other approximations and may not capture the full 5-dimensional space. Models which purport to capture the full 5-dimensional space are too computationally expensive to be utilized. This is particularly exacerbated in the Long Wave Infrared (LWIR), where few BRDF models have been developed and reflections tend toward a more specular response [3].

An ideal HSRS BRDF model would predict effects in the visible, near infrared, short wave infrared (VNIR/SWIR), the mid-wave infrared (MWIR), and LWIR. To adequately capture wavelength responses, the incident light must come from a monochromatic source (e.g. a laser), which are only available at particular wavelengths. Empirical models and BRDF databases attempt to capture all wavelength domains by interpolating between measured wavelengths.

By the same token, laboratory validation of any BRDF model is difficult, both due to the sparsity of monochromatic light sources, and the ability to knowingly generate

surfaces for measurement. Most BRDF models assume that the surface features obey some set of statistics, which can be difficult to knowingly replicate in the laboratory. To that end, numerical simulations of rough surfaces and their reflections may be used to bridge the knowledge gap. Numerical simulation provides wavelength agility, fine control of surface features, and mathematical precision in observation.

1.2 Proposal and Thesis Organization

Fourier techniques offer powerful tools to numerically simulate rough surface reflection. The intention of this work is to develop a full wave-optics simulation of rough surface scatter. A random surface with known Gaussian statistics is generated in order to compare to the well known Modified Beckmann Kirchoff (MBK) model. The scattering from this surface is then propagated to the far field utilizing Fourier techniques and the results are compared to predictions of several BRDF models. Finally parameters for future simulations and experiments are provided.

BRDF models predict the scatter over the angular expanse of the entire hemisphere; ideally validation of these models would consider scatter of the entire angular expanse of the hemisphere. Computational limitations to the detector size and shape in the far field limits the angular extent over which the far field scatter can be simulated. As a result, in this thesis, the angular extent over which the predictive models may be compared is likewise limited.

This thesis will begin with background information in Chapter II, including discussions of electromagnetics, pertinent rough scatter geometry, and a discussion of BRDF model types. Fourier theory pertinent to both the generation of rough surfaces and optical wave propagation will then be discussed in Chapter III, with particular attention given to the various Fourier methods available to propagate the surface scatter and their benefits and drawbacks. Finally results from the simulation are

presented and their comparison to existing models are discussed in Chapter IV. Recommendations for future work are provided in Chapter V.

II. Background

2.1 Electromagnetics

Electromagnetics are described by Maxwell's equations [4]. In MKS units,

$$\nabla \times \vec{E} = -\frac{\partial \vec{B}}{\partial t}, \tag{2.1}$$

$$\nabla \times \vec{B} = \mu \left(\vec{J} + \epsilon \frac{\partial \vec{E}}{\partial t} \right), \tag{2.2}$$

$$\nabla \cdot \vec{E} = \frac{\rho}{\epsilon}, and \tag{2.3}$$

$$\nabla \cdot \vec{B} = 0 \tag{2.4}$$

where $\vec{E}$ and $\vec{B}$ are the electric and magnetic fields, respectively. $\vec{J}$ is current, and ρ is charge density. It is necessary to include a permeability, μ, and a permittivity, ϵ, as material parameters. These equations simplify in free space where $\vec{J} = 0$, $\rho = 0$, $\mu = \mu_0$, and $\epsilon = \epsilon_0$.

With an application of boundary conditions, assuming an infinite, non-conducting, flat surface, Snell's law may be derived. Snell's law is given as [4]

$$n_i \sin(\theta_i) = n_t \sin(\theta_t), \tag{2.5}$$

where n_i and n_t are the indices of refraction and θ_i and θ_t are the angles of incidence and transmission respectively. It can be easily seen for the case of reflection that $\theta_i = \theta_r$, which is known as the law of (specular) reflection. In general, the index of refraction of a material is a complex quantity, $\tilde{n} = n + i\kappa$, which can be related to complex ϵ and μ of the material and free space by [4],

$$n + i\kappa = \sqrt{\frac{\epsilon\mu}{\epsilon_0\mu_0}}, \tag{2.6}$$

where n and κ are the real and imaginary components, respectively. The real component, n, quantifies the refraction at the surface, whereas the imaginary component, κ, quantifies attenuation of radiation propagating in a material.

When polarization is considered at a perfectly flat, infinite, boundary, another set of useful relationships may be derived. Specifically,

$$r_s = \frac{\tilde{n}_1 \cos(\theta) - \tilde{n}_2 \sqrt{1 - \left|\frac{\tilde{n}_1}{\tilde{n}_2} \sin(\theta)\right|^2}}{\tilde{n}_1 \cos(\theta) + \tilde{n}_2 \sqrt{1 - \left|\frac{\tilde{n}_1}{\tilde{n}_2} \sin(\theta)\right|^2}} \tag{2.7}$$

$$r_p = \frac{\tilde{n}_1 \sqrt{1 - \left|\frac{\tilde{n}_1}{\tilde{n}_2} \sin(\theta)\right|^2} - \tilde{n}_2 \cos(\theta)}{\tilde{n}_1 \sqrt{1 - \left|\frac{\tilde{n}_1}{\tilde{n}_2} \sin(\theta)\right|^2} + \tilde{n}_2 \cos(\theta)} \tag{2.8}$$

are the Fresnel equations for reflections of the s and p polarizations, respectively. This work will assume the incident medium has an index of refraction such that $\tilde{n}_1 \approx 1$ is a good approximation. The intensity of the reflections is given by

$$\begin{aligned} F_p(\theta) &= |r_p|^2 \\ F_s(\theta) &= |r_s|^2 . \end{aligned} \tag{2.9}$$

For unpolarized light,

$$F(\theta) = \frac{F_p(\theta) + F_s(\theta)}{2}. \tag{2.10}$$

Note that Snell's law and Fresnel equations hold for idealized surfaces, but solutions to Maxwell's equations for realistic surface may be intractable.

2.2 BRDF

The bidirectional reflectance distribution function (BRDF) quantifies the ratio of the exiting radiance to the incident irradiance and therefore carries units of sr^{-1}. It

was defined by Nicodemus [2] as

$$f_r\left(\hat{\omega}_i, \hat{\omega}_s, \lambda\right) = \frac{L_s\left(\hat{\omega}_i, \hat{\omega}_s, \lambda\right)}{E_i\left(\hat{\omega}_i, \lambda\right)}, \tag{2.11}$$

where $\hat{\omega}_i$ is the incident unit vector, $\hat{\omega}_s$ is the outgoing vector, and λ is the wavelength. The BRDF is a function of wavelength (though some models neglect wavelength). It is informative to consider how the BRDF may be modeled for idealized reflections. For instance, for a monochromatic, perfectly specular reflections, the BRDF could be modeled as

$$f_r\left(\hat{\omega}_i, \hat{\omega}_s\right) = \rho\delta\left(\theta_i - \theta_s\right)\left(\phi_i - \pi - \phi_s\right), \tag{2.12}$$

where the single parameter ρ is the magnitude of the total reflectance and the Dirac delta function δ is unity at the reflectance angle. This relationship is a restatement of the law of specular reflection previously derived from Snell's law for perfectly flat surfaces. For a perfectly Lambertian reflection the BRDF still has only a single parameter

$$f_r\left(\hat{\omega}_i, \hat{\omega}_s\right) = \frac{\rho}{\pi}, \tag{2.13}$$

which would be hypothetically true for a very rough surface and would disperse the total reflectance ρ uniformly over the hemisphere. Realistic surface reflections are rarely well modeled by perfectly specular or perfectly Lambertian reflections, though they may be described as having both diffuse and specular components as seen in Figure 2.1. There exist several classes of BRDF models. Two classes of BRDF models will be discussed herein: microfacet models and scalar wave-optics models. A notable, and intentional, omission is polarimetric (vector) wave-optics models, which will not be discussed.

Figure 2.1. Light incident on a non-ideal surface.

2.3 Microfacet BRDF

One popular class of BRDF models is the microfacet model. The microfacet model assumes geometric optics and is therefore not wavelength dependent. The surface is assumed to have a macrosurface normal pointing in the $\hat{z}$ direction [5]. The microfacet model utilizes both microsurface and macrosurface coordinates. These coordinates were formalized by Rusinkiewicz [6]. As shown in Figure 2.2, $\hat{\omega}_i$ is the unit vector in the direction of the incident macrosurface angle, and $\hat{\omega}_s$ is the unit vector in the direction of the macrosurface scatter. Rusinkiewicz [6] defined a half vector $\hat{\omega}_h$ and a difference vector $\hat{\omega}_d$, such that

$$\hat{\omega}_h = \frac{\hat{\omega}_i + \hat{\omega}_s}{||\hat{\omega}_i + \hat{\omega}_s||}, \tag{2.14}$$

$$\text{and } \hat{\omega}_d = \mathbb{R}_y\left(-\theta_h\right)\mathbb{R}_z\left(-\phi_h\right)\hat{\omega}_i, \tag{2.15}$$

where $\mathbb{R}_a(\beta)$ is a right-handed rotation about the axis by an angle β. The half vector, $\hat{\omega}_h$ represents the microfacet orientation which produces a specular reflection of a given incident and scattered direction. Additionally, the half angle, θ_h, is the angle made by the microsurface normal, $\hat{\omega}_h$, and the macrosurface normal, $\hat{z}$. Rotating the incident vector, $\hat{\omega}_i$, to be in the microsurface coordinate system yield the difference vector, $\hat{\omega}_d$. In turn, the difference angle, θ_d, is the angle made by the difference

vector, $\hat{\omega}_d$, and the macrosurface normal, $\hat{z}$. When calculating Fresnel reflectance, The difference angle θ_d is of particular importance.

Historically, microfacet models have been given qualitative labels: empirical, semi-empirical, or experimental [5]. They could be defined as

$$f_r\left(\hat{\omega}_i, \hat{\omega}_s\right) = \rho_s S\left(\hat{\omega}_i \hat{\omega}_s\right) + \rho_v V\left(\hat{\omega}_i \hat{\omega}_s\right) + \frac{\rho_d}{\pi}, \tag{2.16}$$

where ρ_s, ρ_v, and ρ_d are respectively the specular, volumetric, and diffuse fitting parameters for a surface reflection (S), volumetric reflection (V), and diffuse reflection. Note that the fitting parameters are not charge density ρ from Maxwell's Equations given in 2.4. By using the general form given by Butler [5] as

$$f_r\left(\hat{\omega}_i, \hat{\omega}_s\right) = \rho_s P\left(\hat{\omega}_i \hat{\omega}_s\right) D\left(\hat{\omega}_h\right) F\left(\theta_d\right) G\left(\hat{\omega}_i, \hat{\omega}_s\right) \sigma\left(\theta_i, \theta_s\right) + \rho_v V\left(\hat{\omega}_i, \hat{\omega}_s\right) + \frac{\rho_d}{\pi}. \tag{2.17}$$

The microfacet theory is more readily discussed by identifying the presence or absence of a given term in a given model. Fitting parameters, ρ_s, ρ_v, and ρ_d, in Equation (2.17) remain for specular, volumetric, and diffuse reflections, respectively. From Equation (2.16), S becomes a product of a prefactor $P\left(\hat{\omega}_i, \hat{\omega}_s\right)$, a microfacet orientation distribution $D\left(\hat{\omega}_h\right)$, a Fresnel reflection $F\left(\theta_d\right)$, a geometric attenuation term $G\left(\hat{\omega}_i, \hat{\omega}_s\right)$, and a cross section conversion term $\sigma\left(\theta_i, \theta_o\right)$. A summary of several popular microfacet models is given by Butler in [5].

The Cook-Torrance BRDF model is a popular microfacet model. Like many other microfacet models, it neglects volumetric reflections by setting $\rho_v = 0$. The prefactor, $P\left(\hat{\omega}_i \hat{\omega}_s\right)$, in the microfacet form, Equation (2.17), is a collection of terms exclusive to a given BRDF model. For the Cook-Torrance [7] microfacet model, $P\left(\hat{\omega}_i \hat{\omega}_s\right) = 4$.

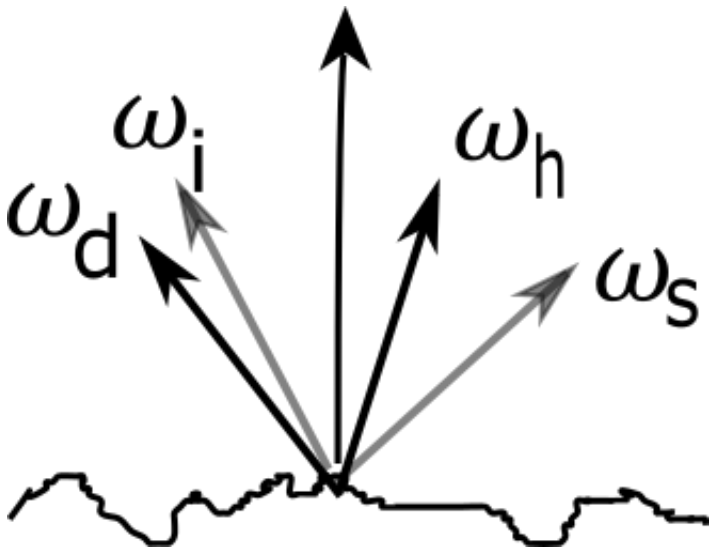

Figure 2.2. Rusinkiewicz coordinate system

The Gaussian microfacet distribution,

$$D\left(\hat{\omega_h}\right) = D_b\left(\theta_h\right) = \frac{1}{\pi m^2 \cos^4\left(\theta_h\right)} \exp\left[-\left(\frac{\tan\left(\theta_h\right)}{m}\right)^2\right], \tag{2.18}$$

is the microfacet distribution function utilized by the Cook-Torrance model. Parameterized only by m, it is similar to the distribution originally formulated in 1963 by Beckmann [8] and is popular amongst other microfacet BRDF models [5], [9],[10]. In addition,

$$F\left(\theta\right) = \frac{F_p\left(\theta\right) + F_s\left(\theta\right)}{2} \tag{2.19}$$

is the familiar Fresnel equation which is utilized by Cook-Torrance. It's worth noting that other microfacet models, including Sandford-Robertson [11], use approximations to the Fresnel equations [5]. A geometric attenuation term

$$G\left(\hat{\omega_i}, \hat{\omega_s}\right) = G_c\left(\hat{\omega}_i, \hat{\omega}_s\right) = \min\left[1, \frac{2\cos\left(\theta_h\right)\cos\left(\theta_s\right)}{\cos\left(\theta_d\right)}, \frac{2\cos\theta_h \cos\theta_i}{\cos\theta_d}\right], \tag{2.20}$$

is utilized by the Cook-Torrance model [7]. This geometric attenuation term was

derived assuming a surface with v-shaped grooves [12]. The first term of the min function occurs when the surface is truly flat and no attenuation is occurring. A minimum occurs for the second term when the incident angle or the microfacet normal is steep with respect to the macrosurface normal, also known as obscuration. Finally, the third term is a minimum when the scatter angle or microfacet angle is steep with respect to the surface normal, also known as shadowing and masking [5]. A cross section conversion term

$$\sigma\left(\theta_i, \theta_s\right) = \frac{1}{4\cos\theta_i \cos\theta_s} \tag{2.21}$$

is also used by the Cook-Torrance model.

2.4 Scalar wave-optics models

Another class of BRDF models is scalar wave-optics models. Unlike the microfacet models, these models do not assume geometric-optics approximation; that is, they include the effects of diffraction and interference. As a result of the wave-optics derivation, these models tend to result in more accurate BRDFs than microfacet models [13]. The main shortcoming of these models is that for an arbitrary surface the models rapidly become computationally intensive and frequently do not result in a closed-form solution. As a result, they are generally inappropriate for use in resource constrained environments.

Here we will focus on a model modified from the Beckmann-Kirchhhoff (BK) scattering model. BK considers only an overall phase shift to the light due to surface roughness, where the microfacet treats the surface as a collection small geometric reflectors. Note that the BK model was developed before the BRDF was defined and therefore is not truly a BRDF. It was modified by Krywonos [14]. In the Modified

Beckman Kirchhoff model (MBK), radiance is given as

$$L_s\left(\theta_s,\phi_s\right) = K\frac{\pi l_c^2 \exp\left(-g\right)}{A_s}\sum_{m=1}^{\infty}\frac{g^m}{m!m}\exp\left(-\frac{v_{xy}^2 l_c^2}{4m}\right), \tag{2.22}$$

where l_c and A_s are the correlation length and area of illumination of the material, respectively. The function g given in Equation (2.22) is a measure of phase variance due to an overall surface roughness σ_s,

$$g = \left(\frac{2\pi\sigma_s}{\lambda}\right)^2\left(\cos\theta_i + \cos\theta_s\right)^2, \tag{2.23}$$

and v_{xy} is given as

$$v_{xy}\left(\theta_i,\theta_s,\phi_s,\lambda\right) = \frac{2\pi}{\lambda}\sqrt{\sin^2\theta_i - 2\sin\theta_i\sin\theta_s\cos\phi_s + \sin^2\theta_s}. \tag{2.24}$$

The infinite sum in Equation (2.22) is not computationally tractable. Krywonos shows in reference [14] the number of terms needed to accurately calculate the BRDF is

$$m_{max} = 1.1 \times g_{max} + 40, \tag{2.25}$$

where g_{max} is the maximum of Equation (2.23). The K term of Equation (2.22) is an overall normalization defined in terms of radiance as

$$K = \frac{\int_{-\infty}^{\infty}\int_{-\infty}^{\infty} L_s\left(\alpha_s,\beta_s - \beta_s d\beta_s d\alpha_s\right)}{\int_{-1}^{1}\int_{-\sqrt{1-\alpha_s}}^{\sqrt{1-\alpha_s}} L_s\left(\alpha_s,\beta_s-\beta_i\right)d\beta_s d\alpha_s} \tag{2.26}$$

and acts as an energy conservation term by accounting for any evanescent waves. However, K is frequently impractical to compute, as it requires some foreknowledge of L_s. The need for K may be avoided in simulation by ensuring that the surface is uniformly illuminated. Butler shows in [3] that a polarization factor Q may be used

in lieu of a Fresnel term. Note that Q is a perturbed Fresnel term such that

$$Q_{ss} = \left| \frac{\left(\tilde{n}^2-1\right)\cos(\phi_s-\pi)}{\left(\cos\theta_i+\sqrt{\tilde{n}^2-\sin^2\theta_i}\right)\left(\cos\theta_s+\sqrt{\tilde{n}^2-\sin^2\theta_s}\right)} \right|^2 \tag{2.27}$$

$$Q_{sp} = \left| \frac{\left(\tilde{n}^2-1\right)\sqrt{\tilde{n}^2-\sin^2\theta_s}\sin(\theta_s-\pi)}{\left(\cos\theta_i+\sqrt{\tilde{n}^2-\sin^2\theta_i}\right)\left(\tilde{n}^2\cos^2\theta_s+\sqrt{\tilde{n}^2-\sin^2\theta_s}\right)} \right|^2 \tag{2.28}$$

$$Q_{ps} = \left| \frac{\left(\tilde{n}^2-1\right)\sqrt{\tilde{n}^2-\sin^2\theta_s}\sin(\phi_s-\pi)}{\left(\tilde{n}^2\cos\theta_i+\sqrt{\tilde{n}^2-\sin^2\theta_i}\right)\left(\cos\theta_s+\sqrt{\tilde{n}^2-\sin^2\theta_s}\right)} \right|^2 \tag{2.29}$$

$$Q_{pp} = \left| \frac{\left(\tilde{n}^2-1\right)\left(\sqrt{\tilde{n}^2-\sin^2\theta_i}\sqrt{\tilde{n}^2-\sin^2\theta_s}\cos(\phi_s-\pi)-\tilde{n}^2\sin\theta_i\sin\theta_s\right)}{\left(\tilde{n}^2\cos\theta_i+\sqrt{\tilde{n}^2-\sin^2\theta_i}\right)\left(\tilde{n}^2\cos\theta_s+\sqrt{\tilde{n}^2-\sin^2\theta_s}\right)} \right|^2 \tag{2.30}$$

$$\text{and } Q = Q_{ss} + Q_{sp} + Q_{ps} + Q_{pp} \tag{2.31}$$

So that when $\theta_i = \theta_s$ Q reduces to the Fresnel equation given by Equation (2.19). Utilizing the perturbed Fresnel term in Equation (2.31), the MBK model may be further modified to

$$f_r\left(\hat{\omega_i},\hat{\omega_s}\right) = \frac{Q\pi l_c^2}{2\lambda^2}\exp\left(-g\right)\sum_{m=1}^{\infty}\frac{g^m}{m!m}\exp\left(-\frac{v_{xy}^2 l_c^2}{4m}\right). \tag{2.32}$$

2.5 BRDF Measurements

Because BRDF values may vary by several orders of magnitude, it is difficult to take measurements accurately over the entire range. Laser illumination of the sample is typically used to ensure highly directional, narrow-band illumination of the material. BRDF measurements may be made at AFIT using the CASI® from Schmitt Measurement Systems (SMS), a division of Schmitt Industries Inc. To isolate the reflectance signal, the CASI® uses a chopper blade and a lock-in amplifier. This reduces deleterious effects from self-emission, particularly in the infrared, as the incident laser beam is chopped at a known frequency whereas any self-emission from the sample is not. The signal may also be amplified at varying levels of gain to ameliorate

detection over several orders of magnitude. A neutral density filter may also be used to control the incident irradiance on the sample.

The CASI®system uses a sample holder centered in a goniometer. Samples are then illuminated by laser light of a particular wavelength and incident angle. A goniometer arm typically scans the detector to obtain in-plane data ($\phi_s = 0$ or $\phi_s = \pi$). Out-of-plane data may be obtained by tipping the sample. Modifications to the AFIT CASI® system allow it to collect polarization information [3]; these modifications will not be detailed here.

2.6 Surface Statistics

Rough surfaces are random and no two rough surfaces are identical, but the surface roughness obeys some higher-order statistics. BRDF models make some assumptions about the statistical behavior of the surfaces they model. Rough surfaces are typically thought of in terms of two parameters: deviation of surface height to some mean reference surface and how frequently these deviations occur across the surface [15],[16],[17].

Deviations from the reference surface are governed by a height probability distribution. Height, h, at a position on the reference surface, $\bar{r}$, is given by the height function $h(\bar{r})$. This height function, $h(\bar{r})$, is governed by the statistical height distribution $p(h)$, where $p(h)\,dh$ is the probability of any surface being between h and dh aways from the reference surface. Reference surface are assigned the height value of zero, in order to result in zero mean surfaces [16], such that

$$\langle h \rangle_s = \int_{-\infty}^{\infty} hp(h)\,dh = 0, \tag{2.33}$$

where the angle brackets indicate a spatial average. This assumption allows for mathematical ease, and surface profile measurements may be adjusted to allow for a zero mean by choosing the reference surface cleverly. The root mean square (RMS) surface height is then defined as the standard deviation of the surface[16], where

$$\sigma = \sqrt{\langle h^2 \rangle_s}. \tag{2.34}$$

Beckmann and Spizzichino [8] state the normal (Gaussian) distribution as, "the most important and typical of a rough surface." A large amount of the rough surface theory assumes a Gaussian distribution of height, that is,

$$p\left(h\right) = \frac{1}{\sigma_h} \exp\left(-\frac{h^2}{\sigma_h^2}\right), \tag{2.35}$$

where the definition of $p(h)$ varies by 2π across the literature. In Reference [16], Ogilvy provides a brief summary in the defense of Beckmann's assertion, as well as some contradictions. Nevertheless, for the purposes of this work, surfaces will be assumed to be both Gaussian distributed and Gaussian correlated.

The deviation of height from the reference surface does not fully describe the surface roughness. The second parameter to be considered is the surface autocorrelation. The correlation describes how correlated the surface heights are across the surface and is most readily observed in Figure 2.3 as the distance between deviations from the reference surface. All three figures have identical RMS surface height of $\sigma_s = 0.5mm$ but varying surface correlation lengths. A Gaussian surface autocorrelation is given by the following expression [14],[16],[17]:

$$ACF\left(x, y\right) = \sigma_h^2 \exp\left[-\left(\frac{(x^2 + y^2)}{l_{cr}^2}\right)\right], \tag{2.36}$$

where l_c is the surface correlation length. The MBK models of both diffracted radi-

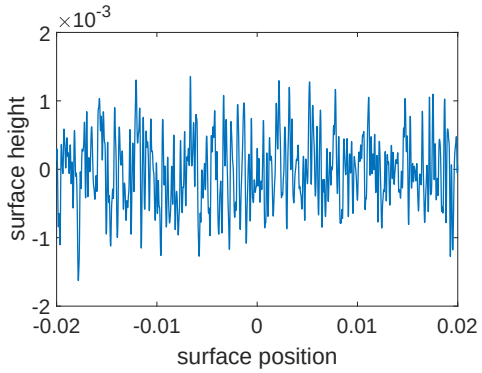

(a) Correlation length, $l_{cr} = 0.1mm$.

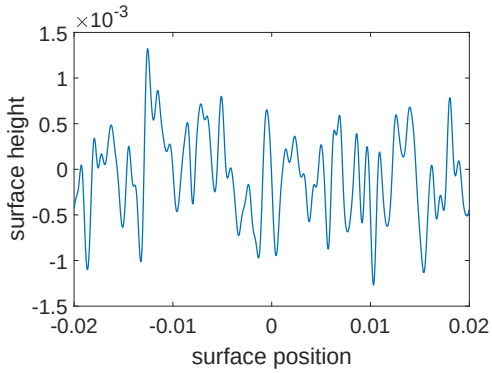

(b) Correlation length, $l_{cr} = 0.5mm$.

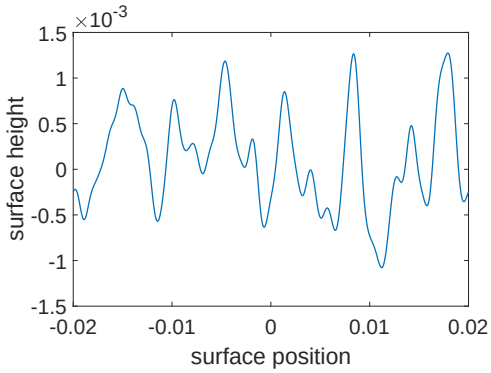

(c) Correlation length, $l_{cr} = 1mm$.

Figure 2.3. Profiles of three random Gaussian surfaces with identical surface height standard deviations of $\sigma_h = 0.5mm$ but varying correlation lengths.

ance and the BRDF make direct use of the rough surface statistics. Note that the microfacet models consider the distribution of surface slopes which could be related to the derivative of the rough surface. The distribution of slopes is derived by Beckmann and Spizzichino [8]. For Gaussian surfaces,

$$p\left(\theta_h\right) = \frac{1}{\sqrt{\pi \tan\left(\beta_0\right) \cos^2\left(\theta_h\right)}} \exp\left(-\frac{\tan\left(\theta_h\right)^2}{\tan\left(\beta_0\right)^2}\right), \tag{2.37}$$

where θ_h is the surface slope and

$$\beta_0 = \frac{(2\sigma_s)}{l_{cr}}. \tag{2.38}$$

For surfaces where the standard deviation is much smaller than the surface slope, $2\sigma << l_{cr}$, the distribution simplifies to

$$p\left(\theta_h\right) = \frac{1}{\beta_0 \pi} \exp\left(-\frac{\theta_h^2}{\beta_0^2}\right). \tag{2.39}$$

While no microfacet distribution directly matches Beckmann's distribution, the distribution for both the Priest microfacet [9],[10], and the Cook-Torrance [7] microfacet models come close [5]. Both will be used as a basis of comparison for simulated data, which will be discussed in Chapter IV.

III. Theory and Methodology

With a background footing of various BRDF models, optical scatter must be produced and quantified to compare to and potentially validate the various BRDF models. This chapter includes:

- discussion of the linear systems theory behind the MBK model of diffracted radiance,
- various methods for generating statistically rough surfaces,
- methods of propagation to the far field,
- and radiometric geometry of the simulation.

3.1 Linear Systems Approach to Surface Scatter

A well defined linear systems approach to rough surface scatter will allow us to utilize computational fourier optics tools to simulate the scatter. Linear systems approaches have previously been used by Harvey in [18] and [19] to show the predictive value of a linear systems approach for wide angle behavior of gratings. Krywonos [14] later shows that diffracted radiance of normal incidence light on a diffracting aperture is given as

$$L\left(\alpha,\beta\right)=\frac{\lambda^2}{A_s}|\mathcal{F}\left\{U_0\left(\hat{x},\hat{y};0\right)\right\}|^2, \tag{3.1}$$

where $\mathcal{F}$ indicate a Fourier transform, U_0 is the complex amplitude distribution emerging from a diffracting aperture, and the 'hat' notation indicates $1/\lambda$ scaling. When the light is incident at other than normal incidence, as illustrated in Figure 3.1 radiance is given as

$$L\left(\alpha,\beta-\beta_0\right)=\gamma_0\frac{\lambda^2}{A_s}|\mathcal{F}\left\{U_0\left(\hat{x},\hat{y};0\right)e^{i2\pi\beta_0\hat{y}}\right\}|^2, \tag{3.2}$$

where α, β, and γ are direction cosines. The direction cosines are related to the spherical coordinates θ and ϕ by the following relationships:

$$\begin{aligned} \alpha &= \sin\theta\cos\phi \\ \beta &= \sin\theta\sin\phi \\ \gamma &= \cos\theta \\ \alpha^2 + \beta^2 + \gamma^2 &= 1, \end{aligned} \tag{3.3}$$

where θ, and ϕ are the polar and azimuthal angles. The squared modulus of the complex amplitude distribution emerging from a diffracting aperture yields the diffracted radiance, rather than irradiance, E, or intensity, I. In contrast to irradiance [20],

$$E\left(x_2, y_2\right) = \frac{1}{\lambda^2 z^2} |\mathcal{F}\left\{U_0\left(x_1, y_1\right)\right\}|_{\xi=\frac{x_2}{\lambda z}, \eta=\frac{y_2}{\lambda z}}|^2, \tag{3.4}$$

radiance over the hemisphere, Equation (3.1), is not restricted to small diffraction angles. Equations (3.1) and (3.2) assume a uniformly illuminated diffracting aperture. To avoid the need for renormalization due to evanescent waves, only cases where the diffracting aperture is uniformly illuminated will be considered.

Computational Fourier techniques are widely published, see for example [21] and [22]. Consider propagation of light diffracting off of some aperture, $U\left(x, y; 0\right)$, its angle spread function (ASF) [20] is given by

$$A\left(f_x, f_y; 0\right) = \int_{-\infty}^{\infty}\int_{-\infty}^{\infty} U\left(x, y; 0\right) \exp\left(-i2\pi\left(f_x x + f_y y\right)\right)\, dx\, dy, \tag{3.5}$$

where f_x and f_y are the Fourier reciprocals of x and y. When Fourier transforms are performed computationally, they are reduced to a set of Riemann sums [21]. Considering first the familiar spatial frequency case, where f_x and f_y are Fourier

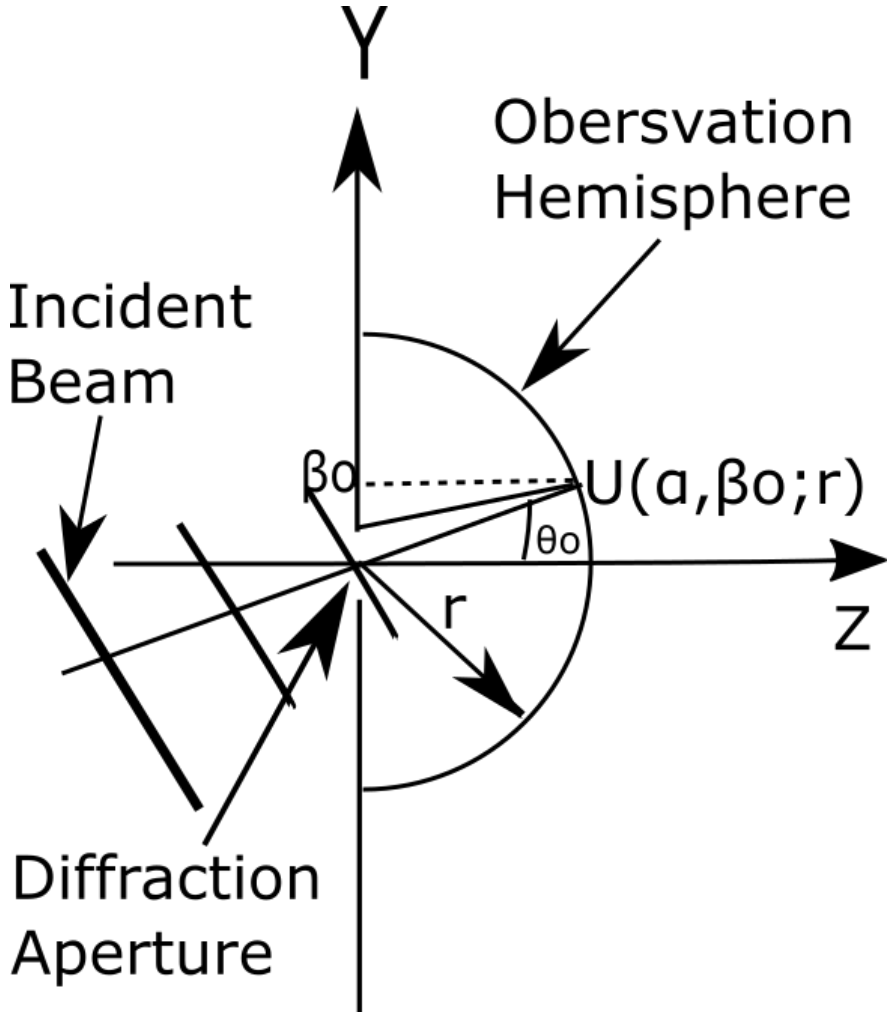

Figure 3.1. Light is incident on a diffracting aperture and an arbitrary angle. The value of β_0 is related to the incident angle θ_0 by Equation (3.3).

reciprocals and are related to the direction cosies, 3.3, by $f_x = \alpha/\lambda$, and $f_y = \beta/\lambda$, the diffracting aperture is represented as a sampled function [21], such that

$$U(x, y; 0) \Rightarrow U(m\Delta x, n\Delta y; 0), \tag{3.6}$$

where Δx and Δy are sample sizes and m and n are indices. The Riemann approxi-

mation is given as [21]

$$\mathcal{F}\left\{U\left(x,y;0\right)\right\} \approx \sum_{m=-\frac{M}{2}}^{\frac{M}{2}-1} \sum_{n=-\frac{N}{2}}^{\frac{N}{2}-1} U\left(m\Delta x, n\Delta y\right) \exp\left(-i2\pi\left(f_x m\Delta x + f_y n\Delta y\right)\right) \Delta x \Delta y. \tag{3.7}$$

The sums result in an approximation of $A\left(f_x, f_y; 0\right)$. By scaling the diffraction aperture variable by $1/\lambda$, the Fourier reciprocals become direction cosines, that is [20],

$$A\left(\alpha,\beta\right) = \int_{-\infty}^{\infty}\int_{-\infty}^{\infty} U\left(\frac{x}{\lambda},\frac{y}{\lambda};0\right) \exp\left(-i2\pi\left(\alpha\frac{x}{\lambda}+\beta\frac{y}{\lambda}\right)\right) d\frac{x}{\lambda}d\frac{y}{\lambda}. \tag{3.8}$$

To obtain $A\left(\alpha,\beta;0\right)$, the sums must be modified similarly to the integrals above. Here, recall that $\hat{x}$ indicates scaling of $\frac{1}{\lambda}$ and the Riemann sum is modified, such that

$$\mathcal{F}\left\{U\left(\hat{x},\hat{y};0\right)\right\} \approx \sum_{m=-\frac{M}{2}}^{\frac{M}{2}-1} \sum_{n=-\frac{N}{2}}^{\frac{N}{2}-1} U\left(m\Delta\hat{x}, n\Delta\hat{y}\right) \exp\left(-i2\pi\left(\alpha m\Delta\hat{x} + \beta n\Delta\hat{y}\right)\right) \Delta\hat{x}\Delta\hat{y}. \tag{3.9}$$

It is worth recalling that since $f_x = \alpha/\lambda$ and $f_y = \beta/\lambda$ [20],

$$\exp\left(-i2\pi\left(f_x m\Delta x + f_y n\Delta y\right)\right) = \exp\left(-i2\pi\left(\alpha m\Delta\hat{x} + \beta n\Delta\hat{y}\right)\right). \tag{3.10}$$

Given Equation (3.10), when using a computation tool like Matlab, so long as the diffracting aperture and grid spacing size are scaled by $1/\lambda$ the transform will result in direction cosine dependence. The two operations are mathematically equivalent. As an example of this scaling, Figures 3.6a and 3.6b provide examples of two square diffracting apertures, both of the same physical size but the second is shown in wavelength scaled coordinates.

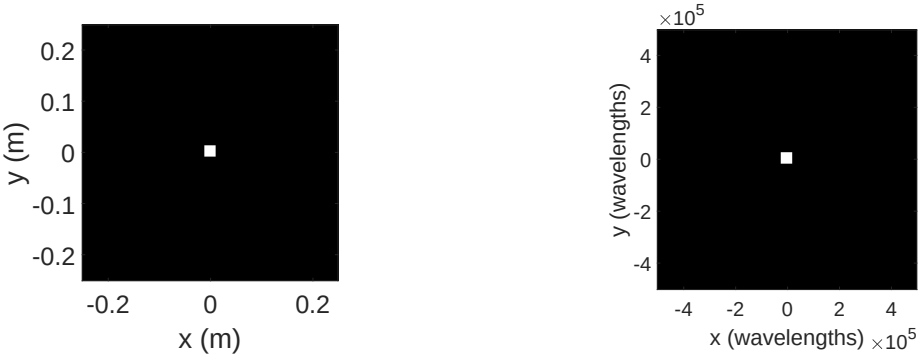

(a) Position coordinates **(b) Wavelength scaled coordinates**

Figure 3.2. Square diffracting apertures in conventional and scaled coordinate systems.

3.2 Experimental and Numerical Approaches

Initially, an experimental approach to measuring the BRDF of a surface was desired. Illustrated in Figure 3.3, a detector would be used to measure the power over the entire hemisphere. One of the principle advantages of this setup is the geometry, the entire hemisphere is readily accessible for in-plane measurement. Additionally, measurement systems like the CASI™ have a significant dynamic range [3]. However at normal incidence, measurements at $\theta_0 = \theta_s$ are not possible, in order to observe the specular lobe of the BRDF shape, normal incidence illumination is avoided.

A numerical wave-optics study has several advantages: wavelength agility, high mathematical precision in simulation, and the ability to readily alter diffracting apertures. The principle drawbacks of a numerical study are the propagation geometry and idealized nature of the simulation. Fourier techniques for optical wave propagation typically propagate between two parallel planes leaving the majority of the hemisphere inaccessible.

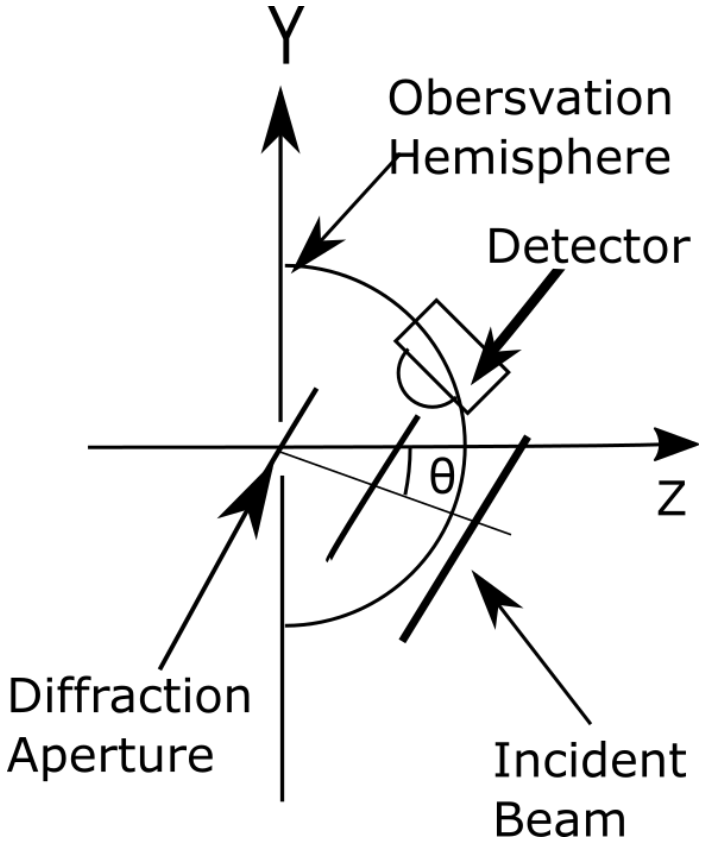

Figure 3.3. Light is incident on a diffracting aperture and an arbitrary angle. A detector is shown sweeping out in-plane measurments of the scatter due to the incident light.

3.3 Surface Statistics

The Modified Beckmann Kirchoff (MBK) model of diffracted radiance, and therefore the MBK model of the BRDF, assumes Gaussian correlated and distributed surface heights. Before any information can be learned about the diffraction characteristics of a such a surface, the surface must be accurately modeled. Commonly referred to as a Gaussian surface, it is defined by two parameters: RMS surface height, σ_h, and surface correlation length l_{cr}. These surfaces have a mean value of zero; thus, the RMS surface height of the surface, σ_h, is the standard deviation of the surface height from the zero mean. It is representative of how 'tall' the 'peaks' and 'valleys' of the surface are. The autocorrelation describes the distance at which the height of one point on the surface is related to the height of another point on the surface. Beyond the correlation length, l_c the surface heights are unrelated. It is representative of the distance between the 'peaks' and 'valleys' on the surface as can be seen in Figure 2.3.

The unnormalized probability height distribution of the surfaces is given as

$$p(z) = \exp\left(\frac{-z^2}{\sigma_h^2}\right), \tag{3.11}$$

where z is the surface height coordinate and σ_h is the standard deviation. The unnormalized autocorrelation function of the surface is given by [14],[16]

$$ACF = \sigma_h^2 \exp\left(-\frac{x^2+y^2}{l_{cr}}\right), \tag{3.12}$$

where x and y are the coordinates of the surface's plane, and l_{cr} is the correlation length of the surface. Another method for describing the surface is the power spectral density (PSD). According to the Wiener-Khintchine theorem [23], the PSD is the

Fourier transform of the autocorrelation function, and is given by [14], [16]

$$PSD = \pi\sigma_h^2 l_{cr}^2 \exp\left(-\pi^2 l_{cr}^2 \left(f_x^2 + f_y^2\right)\right), \tag{3.13}$$

where σ_h is the surface height standard deviation, l_{cr} is the surface height correlation length, and f_x and f_y are the Fourier reciprocals of the surface coordinates x and y, respectively.

The diffraction aperture for the MBK model is given by

$$t\left(\phi\left(x,y\right)\right) = \exp\left(-i\phi\left(x,y\right)\right), \tag{3.14}$$

where $\phi\left(x,y\right)$ is the phase at a given coordinate and is given by

$$\phi\left(x,y\right) = 2kz\left(x,y\right). \tag{3.15}$$

Here, k is the wave number given by $k = \left(2\pi\right)/\lambda$, $z\left(x,y\right)$ is the height at a given (x,y) coordinate, and the factor of 2 is required for reflection. Two approaches to investigating the BRDF of these surfaces were considered: experimental measurements of a known Gaussian surface and simulation of propagation from a known Gaussian surface.

3.3.1 Experimental Surface Generation

To generate a known Gaussian surface experimentally, the use of a spatial light modulator (SLM) was considered. A spatial light modulator (SLM) is an optical device that can be used to impose some spatially varying modulation on impinging light. SLMs are widely available commercially and may be used to control incident

light by modulating amplitude or phase individually, or both amplitude and phase simultaneously. There are also various ways to drive an SLM and various material parameters that can be used to alter the incident light. In this work, we considered an SLM composed of a grid of electrically driven liquid crystals that alter the phase of incident light.

The SLM acts as a phase screen, and does not model a surface directly, but only its relationship to Equation (3.15). SLMs are also very sensitive to wavelength and incident angle. The SLMs available at AFIT are restricted to HeNe laser at 632.8 nm wavelength and angles near normal incidence.

In order to take on this work in the lab, accurate simulation of a Gaussian surface by the SLM would need verification. Ultimately the SLM fell short of the requirements of a Gaussian surface. Recall that the surface is described both by the deviation in height from a zero mean, σ_h, and the correlation of the height of on point on the surface to another l_{cr}. The SLM is a modulo 2π device, like the optical phase in Equation (3.14). This results in phase wrapping, that is, deviations greater than 2π are wrapped back to a value between zero and 2π. Consider a Gaussian distribution with zero mean as shown in Figure 3.4, a modulo 2π phase wrapping would "fold" the distribution back in on itself. That is, at π the distribution would be folded back in, such that 2π lines up with 0, 3π lines up with π, and so on. As the standard deviation increases, this wrapping will cause the distribution to flatten.

The phase distribution is related to the surface height distribution given in Equation (3.11) by Equation (3.15). The distribution is given by

$$p(\phi) = \exp\left(\frac{-\phi^2\lambda^2}{32\pi^2\sigma^2}\right). \tag{3.16}$$

In the case of the phase distribution in Equation (3.15), this happens quite rapidly as shown below in Figure 3.5. As the standard deviation reaches $\lambda/5$, the distribution

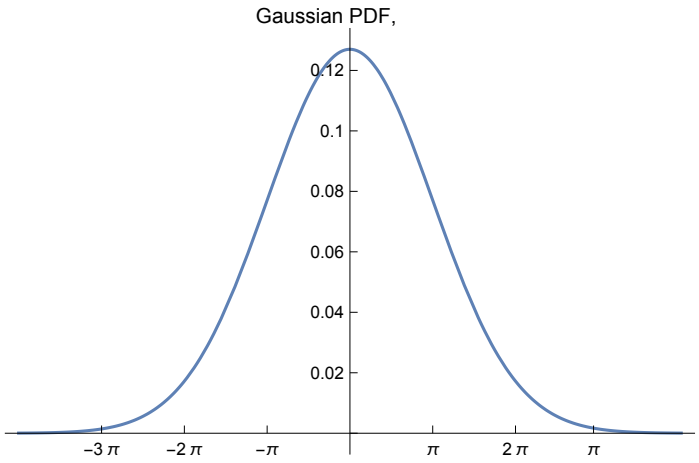

Figure 3.4. A Gaussian Probability Density Function with a standard deviation of π

is almost entirely flat and any Gaussian shape has been lost. To demonstrate this relationship, a vector of 512 random numbers was generated from a normalized half-normal distribution. Use of the half-normal distribution was merely for computational ease. The data generated is shown in the histograms in the left column of Figure 3.5. Then, for each distribution, phase wrapping was done by summing the bin counts of half integer radian sized bins from zero to π. The phased wrapped distribution is shown in the right column of Figure 3.5.

The Wavefront Error (WFE) of the SLM at the wavelength of interest is $\lambda/8$. Note that the first phase distribution was evaluated for $\sigma_h = \lambda/8$ and increased until a flat top distribution was observed at $\sigma_h = \lambda/5$. While it appears there is a limited Gaussian distribution standard deviation that is greater than the WFE of the SLM but sufficiently narrow enough to avoid becoming a flat top, a second issue must also be addressed. The SLM was essentially delta correlated. That is, one pixel's height has no correlation to its neighboring pixels. Recall that the Gaussian surface statistics also assumes a Gaussian correlation. That is, the surface heights are related to neighbors on the same surface up to the surface's correlation length.

3.3.2 Computational Surface Simulation

While wave optics simulations are modulo 2π and subject to the deleterious phase wrapping effects described above, surfaces that capture Gaussian height distribution and correlation can be generated and used to simulated scatter. The transmittance function of a phase screen is given by

$$t(x,y) = \exp\left[i\phi(x,y)\right], \tag{3.17}$$

where $\phi(x,y) = 2kz(x,y)$ is the phase change at a given coordinate. To achieve Gaussian distributed and correlated surfaces, two methods have been implemented with varying levels of success. One method achieves Gaussian correlation of the field, also known as a Gaussian Schell Model (GSM) beam [23], by smoothing a delta correlated array [21]. While it successfully models a GSM beam, limitations on the filter ultimately result in insufficient control of the surface. Details of this implementation can be found in Appendix C.

A second method for simulating Gaussian correlated and distributed surfaces was adapted from methods of generating atmospheric turbulence [22]. Rough surfaces are a random process governed by a certain set of statistics (distribution and correlation). Surfaces may be simulated by generating individual realizations of the random process. The surface $z(x,y)$ is assumed to be Fourier transformable, and may be written as a Fourier transform, such that

$$z(x,y) = \int_{-\infty}^{\infty}\int_{-\infty}^{\infty} \zeta(f_x,f_y)\exp\left(i2\pi\left(f_x x + f_y y\right)\right) df_x df_y, \tag{3.18}$$

where $\zeta(f_x,f_y)$ is the Fourier transform of the surface. Note that $z(x,y)$ is an individual realization of the random surface which is subject to the PSD given in Equation

(3.13). By Parseval's theorem [20],

$$\int_{-\infty}^{\infty}\int_{-\infty}^{\infty}|z\left(x,y\right)|^{2}dxdy=\int_{-\infty}^{\infty}\int_{-\infty}^{\infty}PSD\left(f_{x},f_{y}\right)df_{x}df_{y}. \tag{3.19}$$

Computationally, the surface must be generated on a finite grid. The surface is rewritten as a Fourier series, such that

$$z\left(x,y\right)=\sum_{-\infty}^{\infty}\sum_{-\infty}^{\infty}c_{n,m}\exp\left(i2\pi\left(f_{x_{n}}x+f_{y_{m}}\right)\right), \tag{3.20}$$

where $c_{n,m}$ are the Fourier series coefficients, and f_{x_n},f_{y_m} are the Fourier reciprocals of x and y. Note that the $c_{n,m}$ are complex in general; their real and imaginary parts each have zero mean, equal variances, and zero cross-covariance. That is, they are statistically independent of one another and, as a result, it can be said that they obey circular complex Gaussian statistics. Such statistics can be written as

$$\left\langle |c_{n,m}|^{2}\right\rangle =PSD\left(f_{x_{n}},f_{y_{m}}\right)\Delta f_{x_{n}}\Delta f_{y_{m}}, \tag{3.21}$$

where $\Delta f_{y_m}=1/L_y$ and $\Delta f_{x_n}=1/L_x$ and L_x, and L_y are the x and y side lengths, respectively.

Most mathematical software, like Matlab® , can readily produce arrays of random numbers with zero mean and unit variance of arbitrary size NxN. To generate random draws of $c_{n,m}$ NxN arrays of unit variance random numbers are multiplied by the square root of the PSD. Once $c_{n,m}$ are generated, they are inverse Fourier transformed and the real or imaginary parts are taken, resulting in a surface with the desired statistics. The resulting surfaces match closely with the desired statistics.

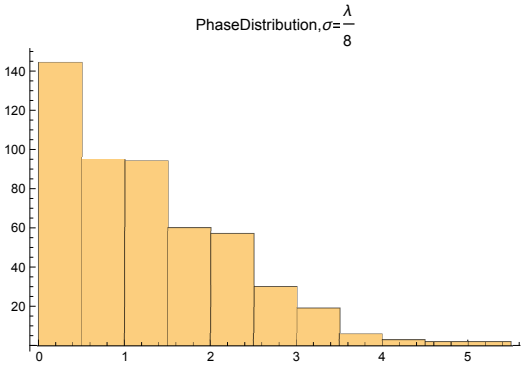

(a) Phase distribution for $\sigma_h = \frac{\lambda}{8}$

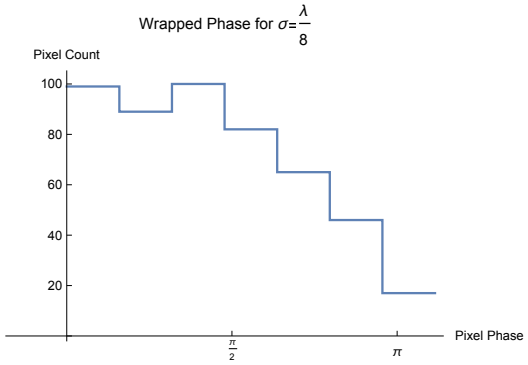

(b) Wrapped phase distribution for $\sigma_h = \frac{\lambda}{8}$

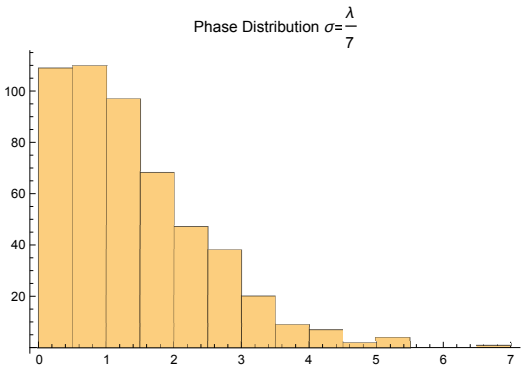

(c) Phase distribution for $\sigma_h = \frac{\lambda}{7}$

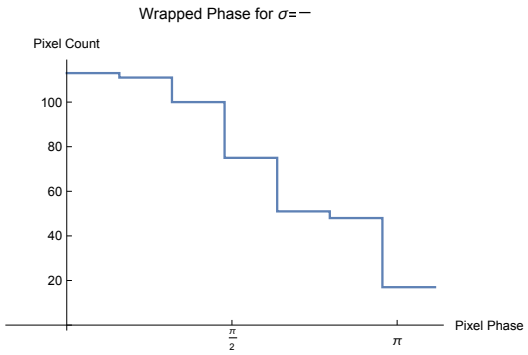

(d) Wrapped phase distribution for $\sigma_h = \frac{\lambda}{7}$

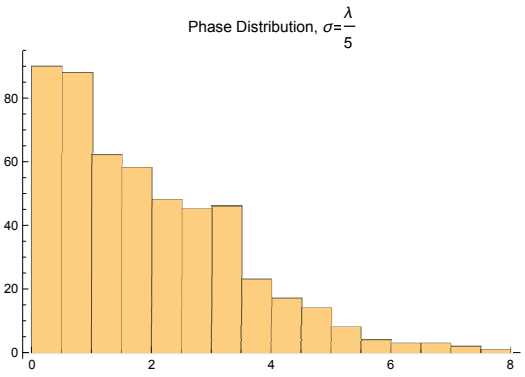

(e) Phase distribution for $\sigma_h = \frac{\lambda}{5}$

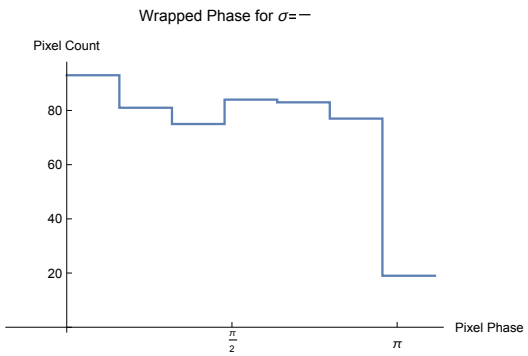

(f) Wrapped phase distribution for $\sigma_h = \frac{\lambda}{5}$

Figure 3.5. A gaussian phase distribution for increasingly rough surfaces (left column) is phase wrapped which reveals a rapid flattening of the distribution (right column). Note that a half normal distribution was utilized rather than a full normal distribution for computational ease.

3.4 Radiance Analysis

Fourier techniques may be used to propagate in direction cosine space and therefore directly calculate radiance [18]. Square diffracting apertures have analytic Fourier transforms which will be used for comparison against computational results. The radiance is given by Equation (3.1). Assuming a unit amplitude plane wave is incident on the diffracting aperture the complex amplitude distribution is given by

$$U(\hat{x},\hat{y}) = t(\hat{x},\hat{y}) = \text{rect}\left(\frac{\hat{x}_1}{2\hat{w}_x}\right)\text{rect}\left(\frac{\hat{y}_1}{2\hat{w}_y}\right). \tag{3.22}$$

As such, the Fourier transform is given by

$$\mathcal{F}\{U(\hat{x},\hat{y})\} = 4\hat{w}_x\hat{w}_y\text{sinc}(2\hat{w}_x\alpha)\,\text{sinc}(2\hat{w}_y\beta), \tag{3.23}$$

where $2\times\hat{w}_x$ and $2\times\hat{w}_y$ are the side lengths of square aperture scaled by λ. That is,

$$2\hat{w}_x \times 2\hat{w}_y = \frac{2w_x}{\lambda}\times\frac{2w_y}{\lambda} = \frac{A_s}{\lambda^2}. \tag{3.24}$$

The radiance is then given as

$$L(\alpha,\beta) = \frac{A_s}{\lambda^2}\text{sinc}^2(2\hat{w}_x\alpha)\,\text{sinc}^2(2\hat{w}_y\beta). \tag{3.25}$$

Given an aperture where $w_x = w_y = 0.011$ and a wavelength of $\lambda = 0.5\mu m$, theory and computation yield the results shown in Figures 3.6a and 3.6b. Note that the double slit and the square aperture both lack phase variation in the diffracting aperture.

As further verification sinusoidal gratings are considered. Modeling sinusoidal gratings requires both a consideration of sampling and an opportunity to simulate a diffracting aperture with other than binary phase. The amplitude transfer function

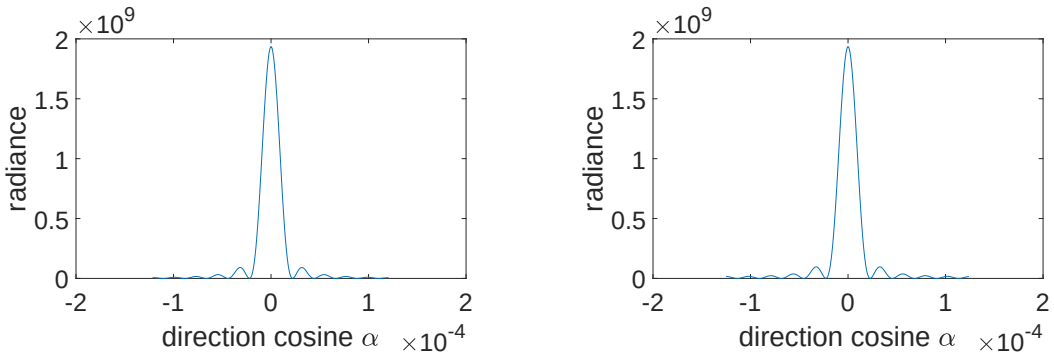

(a) Analytic solution **(b) Computational results**

Figure 3.6. Analytic solutions and computational results are provided for the radiance profile of a square aperture 0.022m in width illuminated with coherent 500nm light

of a cosine varying grating, with length coordinate scaled to $1/\lambda$, is given as

$$t_a = \left(\frac{1}{2} + \frac{m}{2}\cos\left(2\pi\frac{\hat{x}}{\hat{d}}\right)\right)\text{rect}\left(\frac{\hat{x}_1}{2\hat{w}}\right)\text{rect}\left(\frac{\hat{y}_1}{2\hat{w}}\right), \tag{3.26}$$

where m is the amplitude (depth) of the grating, and d is the period. The grating is not infinite so it is truncated by a two dimensional rectangle function, with half width w such that $w = w_x = w_y$. As before, the angle spread function of the grating, in direction cosine space, is given by the Fourier transform of the amplitude transfer function, which is given by:

$$A(\alpha,\beta) = \frac{4\hat{w}}{2}\text{sinc}(2\hat{w}\beta)\left(\text{sinc}(2\hat{w}\alpha) + \frac{m}{2}\text{sinc}\left(2\hat{w}\left(\alpha - \frac{1}{\hat{d}}\right)\right) + \frac{m}{2}\text{sinc}\left(2\hat{w}\alpha + \frac{1}{\hat{d}}\right)\right). \tag{3.27}$$

The radiance is then given as

$$L(\alpha,\beta) = \frac{\lambda^2}{4w^2}|A(\alpha,\beta)|^2, \tag{3.28}$$

where $4w^2$ is unscaled area of the diffracting aperture and λ is the incident wavelength. The analytic solution and computational results show good agreement as seen in Figures 3.7a and 3.7b.

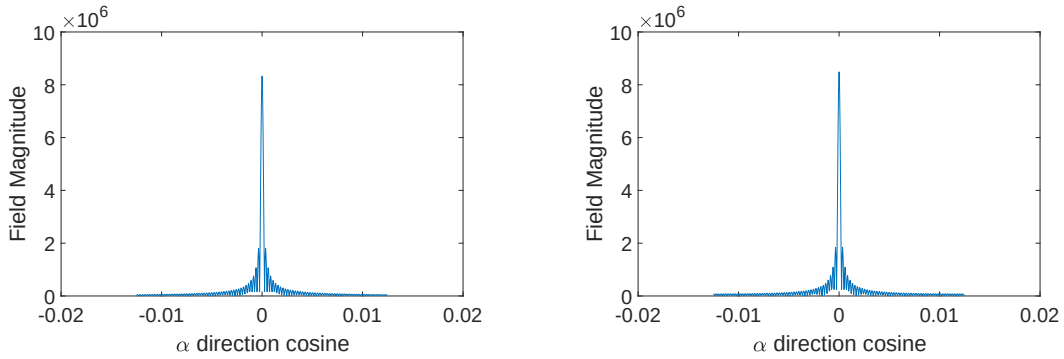

(a) Analytic solution **(b) Computational results**

Figure 3.7. Analytic solutions and computational results are provided for the field magnitude profile of a diffraction grating defined by Equation (3.26) illuminated with coherent 500 nm light.

3.5 Irradiance Analysis

While Section 3.4 showed that a radiance analysis is possible computationally, an irradiance analysis may be more desirable. While wide angle diffracted radiance may be captured exactly with Fourier techniques as shown in References [14], [18], and [19], to observe wide angle behaviors, a hemispherical detector would be required. The accuracy of a hemispherical observation space as a predictive tool has been published [19], but is non-trivial to implement computationally. Practically, our computational Fourier techniques restrict the detector to a plane parallel to the diffracting aperture centered on the propagation axis. This restriction implies a small angle requirement (restricted to angles where a plane may approximate a hemsiphere) as illustrated in Figure 3.8.

Irradiance is a more native quantity to this geometry, and as will be shown in Section 3.6, conversion to radiance is straightforward. For these reasons, an irradiance analysis has a much desired practicality, as not only is it well suited for the geometry, but Fourier techniques for wave propagation are well known and widely published. There are various methods that may be implemented for propagation to the far field, and they result in certain advantages and disadvantages.

3.5.1 Fraunhofer Techniques

The Fraunhofer diffraction integral is given as [20]

$$U(x_2, y_2) = \frac{\exp(ik\Delta z)\exp\left(i\frac{k}{2\Delta z}(x_2^2 + y_2^2)\right)}{i\lambda\Delta z} \times \int_{-\infty}^{\infty}\int_{-\infty}^{\infty} U(x_1, y_1)\exp\left(-i\frac{k}{\Delta z}(x_1x_2 + y_1y_2)\right) dx_1\, dy_1 \tag{3.29}$$

and is valid when

$$\Delta z > \frac{2D^2}{\lambda}, \tag{3.30}$$

where D is the diameter of the diffracting aperture, λ is the wavelength of the light incident on the aperture, and Δz is the propagation distance. When Δz meets the criteria set by Equation 3.30, it is said to be in the far field (also known as the far zone or Fraunhofer zone). Equation 3.29 may be recast in terms of a discrete Fourier transform [20],[21],[22],

$$U(x_2, y_2) = \frac{\exp(ik\Delta z)\exp\left(i\frac{k}{2\Delta z}(x_2^2 + y_2^2)\right)}{i\lambda\Delta z}\mathcal{F}\{U(x_1, y_1)\}|_{f_{x1}=\frac{x_2}{\lambda\Delta z}, f_{y1}=\frac{y_2}{\lambda\Delta z}}. \tag{3.31}$$

One of the advantages of a Fraunhofer approach is computational speed, as Fraunhofer propagations are performed in a single step and therefore are accomplished rapidly [21],[22]. The disadvantage of a Fraunhofer propagation is a lack of control over far field sampling and detector size. Because Fraunhofer propagation is accomplished in a single step, the detector size is determined by the sampling rate in the far field. If the sampling rate of the aperture is given as δ_1 after Fraunhofer propagation the far field sampling is

$$\delta_2 = \frac{\lambda\Delta z}{N\delta_1}, \tag{3.32}$$

where Δz is the propagation distance, N is the number of grid points, and λ is the wavelength of light incident on the aperture. Then the far field detector size is given

as $N \times \delta_2$. For the application of this thesis, Equation 3.32 may result in sample sizes on the order of meters, which obscures the shape of the far field scatter.

3.5.2 Fresnel Propagation

While ultimately the scattered light needs to be propagated to the far field such that the propagation distance Δz satisfies Equation 3.30, utilizing Fresnel propagation techniques allows for greater control over far field sampling and detector size. This flexibility comes at the cost of computational speed. As such, Fresnel propagation falls under two categories: Fresnel Integral and Fresnel Convolution. The Fresnel Integral is given as

$$\frac{\exp(ikz)}{i\lambda\Delta z}\int_{-\infty}^{\infty}\int_{-\infty}^{\infty}U(x_1,y_1)\exp\left(\frac{ik}{2\Delta z}\left[(x_2-x_1)^2+(y_2-y_1)^2\right]\right)dx_1\,dy_1, \quad (3.33)$$

and may be solved directly (the Fresnel Integral form). Alternatively, the convolution form is given as

$$U(x_2,y_2) = U(x_1,y_1)\otimes\left[\frac{\exp(ik\Delta z)}{i\lambda\Delta z}\exp\left(i\frac{k}{2\Delta z}\left(x_1^2+y_1^2\right)\right)\right]. \quad (3.34)$$

Were two Fourier transforms may be used to evaluate Equation (3.34) via the convolution theorem [20]. As outlined by Schmidt in Reference [22], there are tradeoffs between the two forms in terms of computation speed. The convolution form may also be performed in an arbitrary number of steps. While this further reduces computation efficiency, it does allow for significant control over both the farfield detector size and geometry. A thorough derivation of this result may be found in Reference [22]. WaveProp™, a Matlab® toolbox developed by the Optical Sciences Company, is readily able to propagate an arbitrary aperture to the farfield utilizing the convolution form of the Fresnel integral with built-in sampling constraints [24]. For computational

ease as well as far field detector size and sampling control, propagation via Fresnel convolution was implemented in this thesis.

3.5.3 Aliasing

Aliasing is a deleterious effect that is common to any sampled measurement [20],[21],[22]. Sampling a feature too infrequently results in inaccurate or "aliased" results in the observed field. To prevent aliasing from undersampling, the surface was sampled at least ten times per correlation length so as to exceed the Nyquist requirements [20].

Aliasing may also occur in wave propagation due to a wrap around effect. That is, energy that would exist beyond the boundary of the grid, due to diffraction, wraps back around to the center of the grid. This obscures the actual shape of the propagation. To prevent this, absorbing boundaries or guard bands are often used to attenuate any stray light that may wrap back into the observation plane. While several exotic methods of attenuation are published [22], zero padding is sufficient for the purposes of this work.

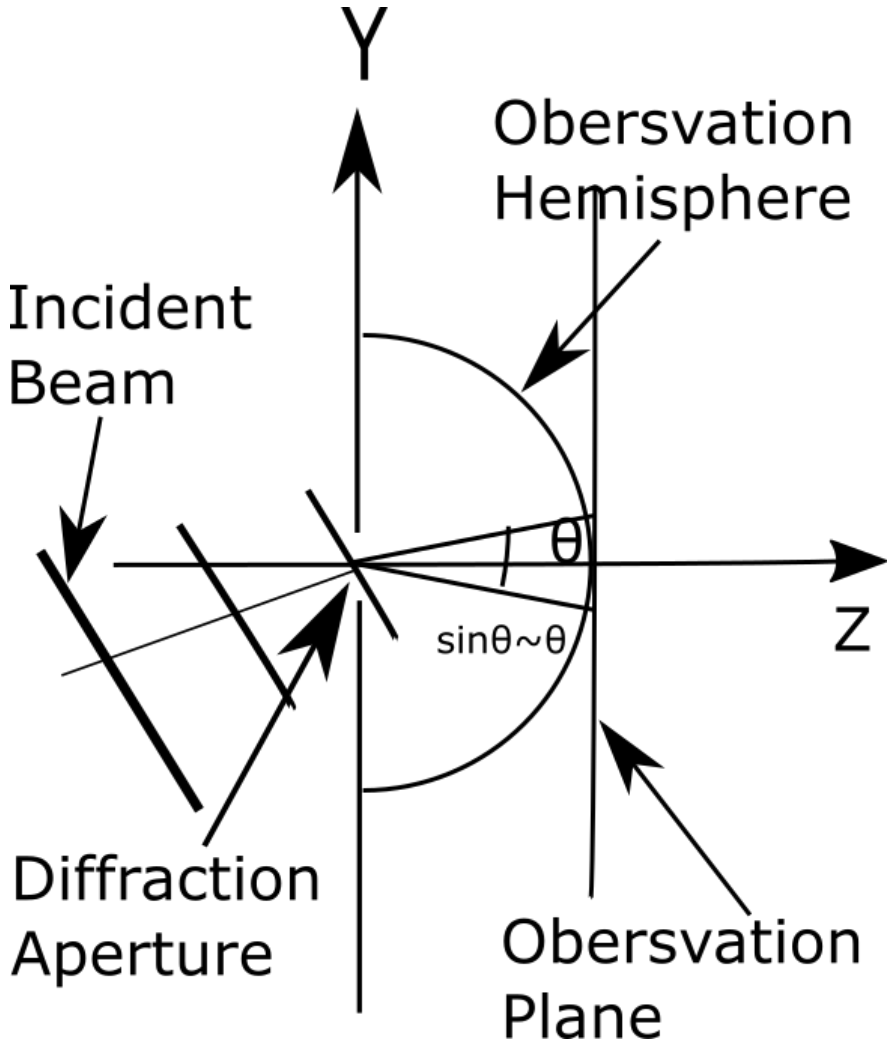

Figure 3.8. Light is incident on a diffracting aperture and an arbitrary angle. The value of β_0 is related to the incident angle θ_0 by Equation (3.3), a planar detector in the far field is placed parallel to the diffracting aperture. The angle markers show the limited angular space where the plane well approximates the hemispherical detector.

3.6 Radiometric Conversion

Fortunately, the conversion to radiance is fairly straight forward for this geometry. Radiance is the fundamental unit of radiometry and is defined within a double differential as [25]

$$\partial^2 P = L\left(x, y\right) \partial\omega_s \partial A_d \cos\left(\theta_d\right), \tag{3.35}$$

where P is power, ω_s is the source solid angle, A_d is the area of the detector, and θ_d is the angle of the detector to the optical axis. Considering the geometry of Figure 3.8 and integrating Equation (3.35) with respect to source solid angle yields the irradiance, given as

$$E = \frac{\partial P}{\partial A_d} = \int_{\omega_s} L \cos\left(\theta_d\right) \partial\omega_s. \tag{3.36}$$

The source solid angle may be rewritten as

$$\partial\omega_s = \frac{\partial A_s \cos\left(\theta_s\right)}{r^2}, \tag{3.37}$$

where A_s is the source area, θ_s is the angle made by the source and the observation axis, and $\theta_d = 0$ on the hemisphere. Equation (3.36) may be recast as

$$E = \frac{\cos\left(\theta_s\right)}{r^2} \int_{A_s} L \, \partial A_s. \tag{3.38}$$

When the aperture is uniformly illuminated, at normal incidence, the irradiance is not dependent on the position of the source, and Equation (3.38) reduces to

$$E\left(x, y\right) = \frac{A_s}{r^2} L\left(x, y\right). \tag{3.39}$$

IV. Results and Analysis

The principle contributions in this thesis work are,

- the development and validation of a rough surface scatter model,
- the comparison of rough surface scatter to two BRDF models,
- the parameterization of future experiment and modeling requirements.

This section will discuss the results which constitute these listed contributions.

4.1 Development and Validation of a Rough Surface Scatter Model

Recall that rough surfaces generate speckle, i.e., areas of constructive and destructive interference, from wavelength scale structures on rough surfaces. A BRDF quantifies where the scattered power goes. In order to perform any sort of parametric investigation, several tasks must be accomplished, including:

- the generation of random surfaces with known statistics,
- the identification and development of appropriate techniques for far field propagation,
- the determination of appropriate propagation parameters (wavelength, propagation distance, surface height standard deviation, surface correlation, number of realizations required for statistical significance).

This section will discuss the development and verification of these tasks.

4.1.1 Generation of Random Surfaces

The ability to repeatedly generate statistically rough surfaces, that is a randomly rough surface governed by a known set of statistics, is needed to investigate the surface scatter. Therefore, the first step of developing a rough surface scatter model is developing numerical methods to generate these surfaces. For comparison to the MBK models of diffracted radiance, and the BRDF, surfaces with a Gaussian height distribution and a Gaussian surface correlation were chosen.

Two methods were considered for generating these surfaces. The theory for these were presented in greater detail in Section 3.3.2. The first method attempted was specific to the generation of Gaussian correlated amplitude transmittance and the results are summarized in Appendix C.

A second, more general, method was implemented. This second method, is more flexible and can be used for any random process described by a PSD. This method utilizes Monte Carlo draws to create individual realizations of the Fourier coefficients of the surface. Utilizing the PSD for a Gaussian correlated and distributed surface, given by Equation (3.13) and restated here, for convenience:

$$\text{PSD} = \pi\sigma_h^2 l_{cr} \exp\left(-\pi^2 l_{cr}^2 \left(f_x^2 + f_y^2\right)\right). \tag{4.1}$$

Note that several Fourier coefficient draws were made. Averaged over many individual realizations, the correlation behavior emerges and as can be seen in Figure 4.1. The results agree very nicely with theory. Additionally, even a single instance of a phase screen results in the expected surface height distribution as can be seen in Figure 4.2.

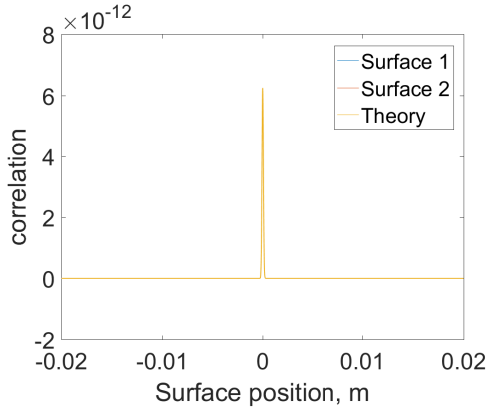

Figure 4.1. The surface autocorrelation of two independent surfaces is averaged over 250 instances of the surface. The average autocorrelation is plotted against the theoretical autocorrelation.

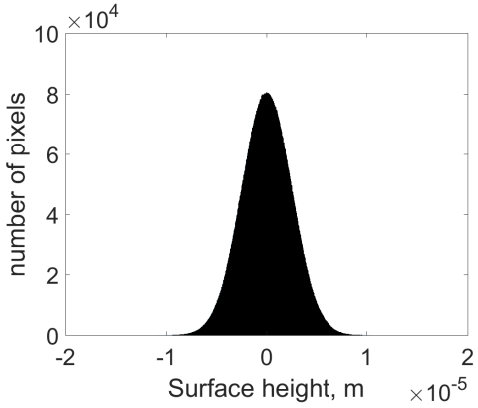

Figure 4.2. A histogram of the surface height of an individual instance of a rough surface with surface height standard deviation of $\sigma_h = 2.8\mu m$ is plotted revealing a Gaussian distribution.

4.1.2 Techniques for far field propagation

With the ability to generate instances of a random surface, techniques for propagating to the far field must be developed. As was discussed in Section 3.5, there are several computational methods for propagation to the far field. Fraunhofer methods allow propagation in a single step, which is highly computationally efficient. However, it results in no control over detector size and sampling rates in the far field. The sampling rates are restricted to the following grid space:

$$\delta_2 = \frac{\lambda \Delta z}{N \delta_1}, \tag{4.2}$$

where λ is the wavelength of the incident light, Δz is the propagation, N is the number of samples in the NxN array, and δ_1 is the target-plane sampling. For relevant parameters this forces the sample size to several meters, making it inappropriate for our application.

Two-step and multi-step Fresnel propagation allows for greater control of both the detector size and sampling rates. Typically, Fresnel propagations either directly

solve the Fresnel diffraction integral, or the Fresnel diffraction integral in convolution form. Both methods ensure propagation using an arbitrary number of steps and therefore exhibit some control over far field sampling. Ultimately, the decision to use the convolution form was for computational convenience. The WaveProp™ tool box for Matlab® solves the convolution form of the integral and has an easily accessible object oriented interface [24].

To propagate to the far field, an instance of the random surface was generated. The surface is surrounded by a a guard band of zeros to prevent aliasing in the far field as discussed in Section 3.5.3 and this zero padding is shown in Figure 4.3a. Note that it was assumed that the sufrace was uniformly illuminated by a unit amplitude plane wave. The scattered light was then propagated to the far field, as shown in Figure 4.3b, using an instance of PropConvolve™ to solve the convolution form of the Fresnel diffraction integral for the given instance. The propagation results in the irradiance in the far field. The irradiance of a statistically significant number of instances was then averaged.

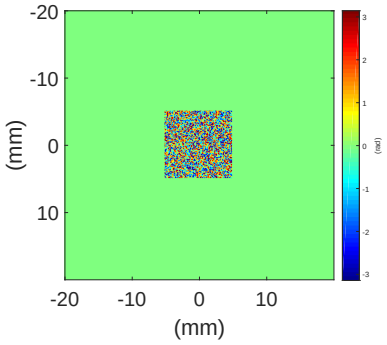

(a) Single realization of the target plane of a surface with $\sigma_h = 2.5\,\mu m$, $l_{cr} = 100$, with a guard band sized 4x larger than the aperture.

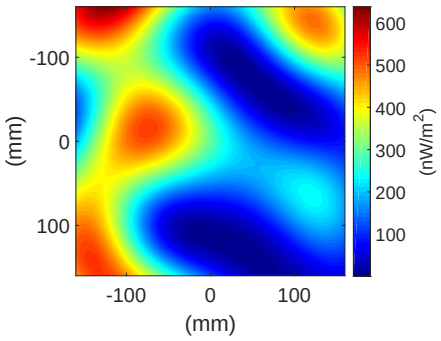

(b) Single realization of the scattered irradiance in the observation plane of a surface with $\sigma_h = 2.5\,\mu m$, $l_{cr} = 100$, and $\lambda = 3\,\mu m$

4.1.3 Simulation Parameters

Provided the results of Figures 4.3a and 4.3b, attention may be turned to the parameters of the simulation. There are three parameters that may be altered to elicit different far field response including the wavelength (λ) of the incident light, the surface height standard deviation (σ_h), and surface correlation length (l_{cr}). Choices for wavelength will be restricted by far field sampling and choices for correlation length will be restricted by target sampling, as well as the desire to keep the simulations reflective of physical reality. Prevailing wisdom indicates that ideal sampling for a Gaussian correlated and distributed surface is somewhere between 10-40 samples per correlation length. A $1\,cm$ sample and a $4\,cm$ guard-band, sampled 4096 times, yields a sample size of $9.76\,\mu m$, making the minimum desired correlation length $100\,\mu m$.

Propagation distance must be sufficiently large to result in far field propagation, which is function of wavelength and aperture size. Detector size should be maximized to capture as large of an angle space as possible, but cannot violate the sampling requirements, which are a function of wavelength, aperture size, and propagation distance.

For binary apertures or mirrors, the distance to the far field is simply the well known relationship:

$$z >> \frac{k\left(x^2 + y^2\right)}{2}, \tag{4.3}$$

which for a square aperture reduces to

$$z >> kx^2. \tag{4.4}$$

For a rough surface, the diffraction behavior of interest comes from structure significantly smaller than the aperture. Following the conclusion of Reference [26], the

propagation distance was set to

$$z >> kxl_{cr}, \tag{4.5}$$

resulting in a much shorter propagation distance and potentially allowing a detector which would envelope a much larger solid angle. Subfigure a of Figure 4.4 shows that this propagation distance is inadequate. The 'pedestal' behavior is of indicative Fresnel ringing, indicating that propagation is terminating in the near field.

To reach the far field, a propagation distance that satisfies the more conventional Fresnel number requirement was used. The Fresnel number is given as

$$N_f = \frac{w^2}{\lambda z}, \tag{4.6}$$

where w is the half width of the apertured surface. To ensure propagation to the far field, z was chosen such that $N_f \leq 0.01$. Figure 4.4 shows progression to the far field, with the width of the original aperture superimposed. The 'pedestal-like' behavior smooths out, and aberrations from the surface roughness can be seen in the far field irradiance pattern in Figure 4.5.

The surface utilized to generate Figures 4.4 and 4.5 had an RMS surface height of $\sigma_h = 2.5\,\mu m$, a correlation length of $l_{cr} = 100\,\mu m$, and an incident wavelength of $\lambda = 6\,\mu m$, which for the MBK model would qualify as a moderately rough surface [14]. While mild aberrations can be seen in the far field in Figure 4.5, speckle is not observed in the far field, and for an average of 250 instances of the far field, aberrations are completely washed out, leaving just a far field pattern of a square mirror. This behavior has been previously observed [27]. To capture the diffraction behavior of the rough surface scatter, the simulation needs to operate in a regime where the far field is dominated by speckle rather than specular reflection.

Figure 4.6 shows that as σ_h approaches $\lambda/2$ the central lobe of the far field pattern

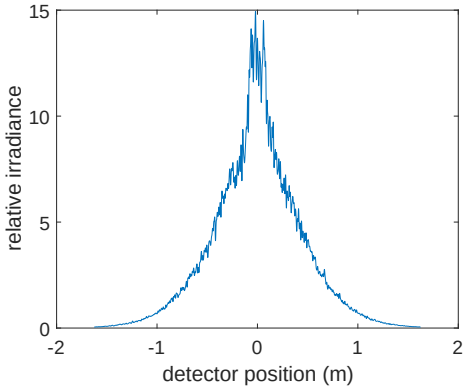

(a) Irradiance Pattern at z=1m exhibits Fresnel ringing resulting from observing the scatter after insufficient propagation

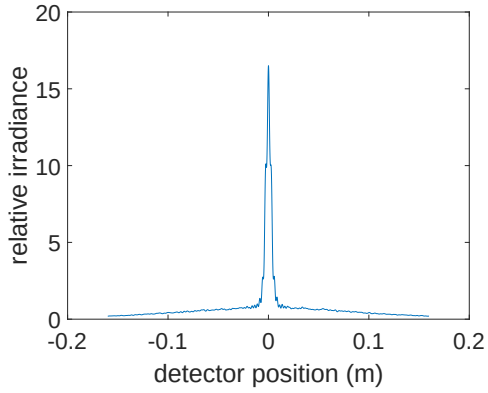

(b) Irradiance Pattern at z=5m exhibits Fresnel ringing, though less extreme than in Figure 4.4a, resulting from observing the scatter after insufficient propagation

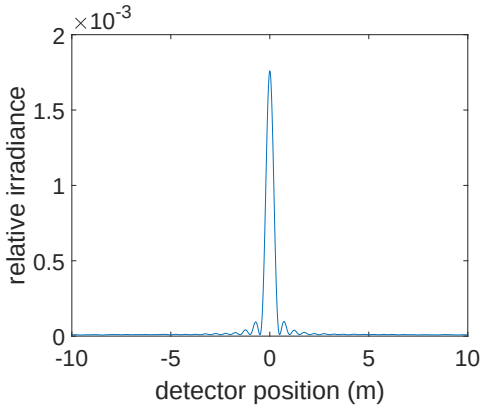

(c) Irradiance Pattern at z=1000m no longer exhibits Fresnel ringing, indicating that observation is occurring in the far field

Figure 4.4. Observed irradiance as the observation plane.

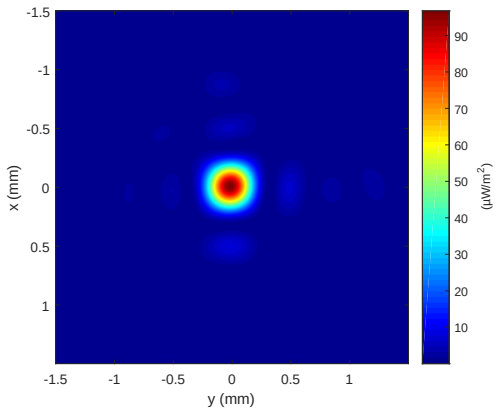

Figure 4.5. Full observation plane for $\sigma_h \approxeq \lambda/3$, averaged over 250 instances. While some mild aberrations are observed, there isno speckle in the far field.

begins to broaden and speckle is more apparent. The pattern is not dominated by speckle until $\sigma_h > \lambda/2$ [27].

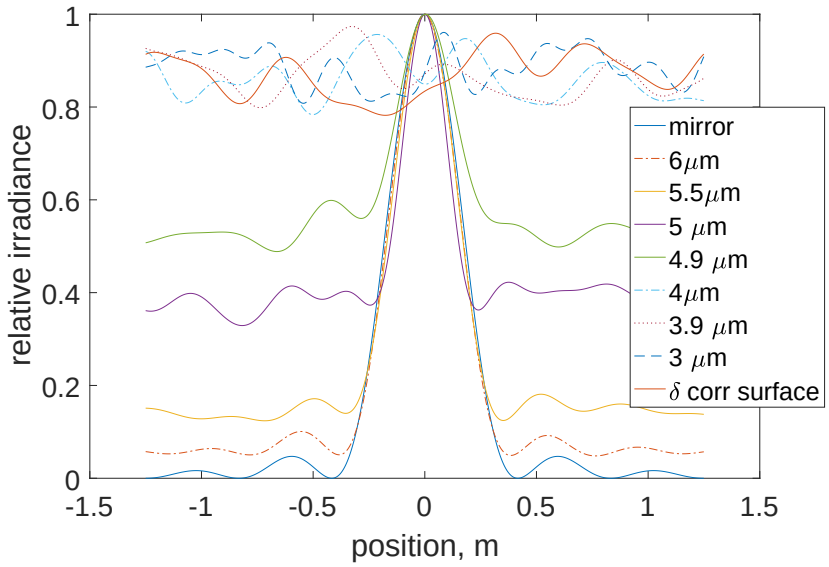

Figure 4.6. Far field irradiance of a surface with standard deviation $\sigma_h = 2.5\mu m$, correlation length $100\mu m$, and various wavelengths. The irradiance is dominated by specular reflections until $4\,\mu m$ when speckle begins dominating the far field.

The observed irradiance in the far field must be averaged over many instances to identify the envelope of scatter. To ascertain whether a significant number of instances had been evaluated, an average power in the bucket (PIB) measurement was taken.

Assigning an arbitrary 'bucket,' as shown in Figure 4.7, the total irradiance within the bucket was calculated and the average taken for each instance. Figure 4.8 shows the PIB as a function of the number of instances. It can be seen that by 250 instances, the average PIB has leveled off, and therefore, the average irradiance is statistically representative.

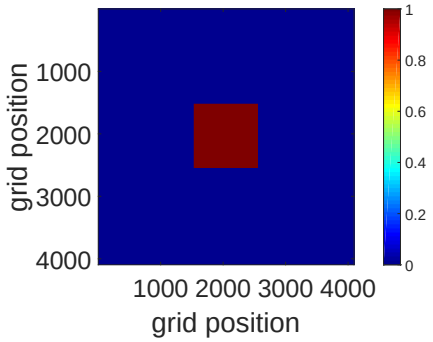

Figure 4.7. "Bucket" utilized for power in the bucket measurements.

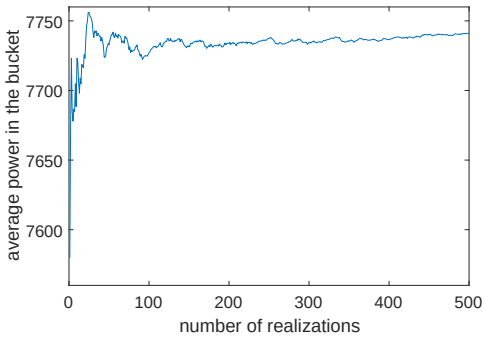

Figure 4.8. Power in the Bucket as a function of the number of realizations

4.2 Comparison of Rough Surface Scatter to BRDF Models

As discussed in Section II of this thesis, two popular categories of the BRDF models are physical optics models and microfacet models. In this section, the results of the rough surface scatter are compared to BRDF model predictions. The BRDF is defined in Equation (2.11) [2] and restated here for convenience

$$f_r\left(\hat{\omega_i}, \hat{\omega_s}, \lambda\right) = \frac{L_s\left(\hat{\omega_i}, \hat{\omega_s}, \lambda\right)}{E_i\left(\hat{\omega_i}, \lambda\right)}. \tag{4.7}$$

In the case of the simulation, the incident irradiance $E_i\left(\hat{\omega_i}, \lambda\right)$ is one, because the incident light is a unit amplitude plane wave. Therefore, $f_r\left(\hat{\omega_i}, \hat{\omega_s}, \lambda\right) = L_s\left(\hat{\omega_i}, \hat{\omega_s}, \lambda\right)$, and as was shown in the Section III, $L_s\left(\hat{\omega_i}, \hat{\omega_s}, \lambda\right) = z^2 * E_s\left(\hat{\omega_i}, \hat{\omega_s}, \lambda\right)$ for the geometry of the rough surface simulation, Which is to say that the BRDF is equal to the diffracted irradiance with an overall constant normalization. By normalizing both the

BRDF and the diffracted irradiance to a unit maximum amplitude, direct comparison may be made between the BRDF and the diffracted radiance calculated in the simulation. While there may be scenarios in which differences in overall magnitude may be of interest, here the comparison is being made between the overall shape or envelope of the functions. Therefore, absolute units will not be indicated on the comparison charts, rather they will be labeled, "relative irradiance," and arbitrary units of irradiance are to be assumed. While the BRDF models predict the behavior for the entire hemisphere, only the in-plane slice will be compared. The in-plane slice is the portion most closely approximated by a flat detector, and is also the most likely measurement done with an experimental apparatus.

For consistency of comparison, both models used assume a Gaussian distributed and correlated surface. The physical optics model used is the MBK model, and the geometric model used is the microfacet model. In reference [14] an analytic radiance for a Gaussian distributed and correlated surface are defined, and are used for comparison below.

As discussed in Section III of this thesis, due to both angular approximations and sampling requirements, the far field detector in the simulation can envelope only a small fraction of the total scattering hemisphere. As a result, 'verification' of the models used for comparison is not claimed. The less satisfying qualifier of consistency with the compared model is used in lieu of verification.

Figure 4.9 shows the predicted irradiance from the MBK model for several wavelengths with a consistent surface height standard deviation and correlation length. While it is a small variation, there is a noticeable variation across the detector aperture. Figure 4.10 shows direct comparison of average irradiance with the predicted MBK results for a surface height standard deviation $\sigma_h = 2.5\mu m$, and surface correlation length $l_{cr} = 100\mu m$. Figure 4.10a shows that for incident light having a

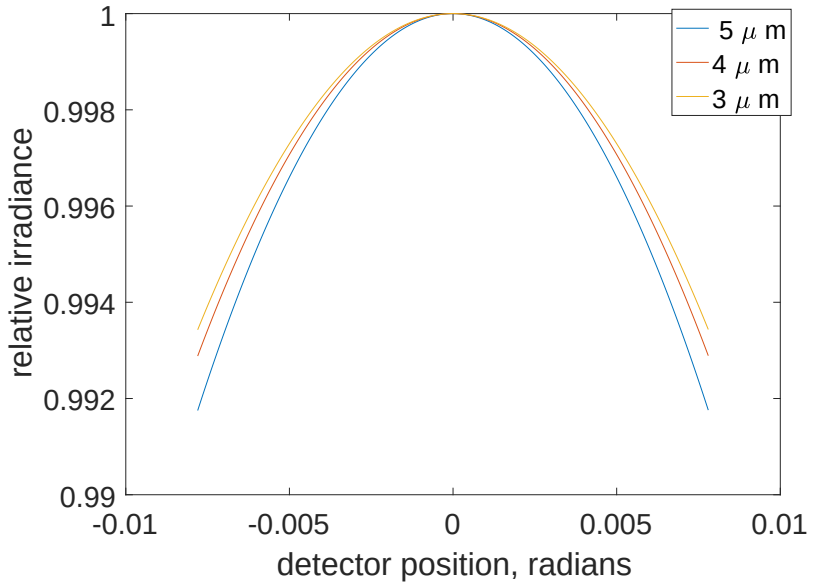

Figure 4.9. In-plane predictions of the irradiance from the MBK model show a slight but noticeable variation in the irradiance envelope across the aperture as well as a variation in wavelength.

wavelength of $\lambda = 5\mu m$ the scatter is in a regime still dominated by specular reflection and is not consistent with MBK. However, Figures 4.10c and 4.10b, where incident light is of wavelength $\lambda = 3\,\mu m$ and $\lambda = 4\,\mu m$ respectively, are in regions dominated by speckle and are consistent with predicted MBK results.

A second simulation was taken for the same surface parameters and wavelength $\lambda = 3\,\mu m$ ignoring the sampling requirements and broadening the detector to double its size. While knowingly risking aliasing in the far field, Figure 4.11 shows that as the detector size increases, and therefore increases the angle space observed increases, the results continue to be consistent with MBK, giving further confidence that in regimes dominated by speckle, MBK is a useful predictive tool.

Figure 4.12 shows an anomalous behavior with respect to the surface's correlation length. As the correlation length increases for a surface in a regime dominated by a specular response, but that does include some speckle, the irradiance in the far field becomes more specular. While no quantitative explanation is offered, a qualitative

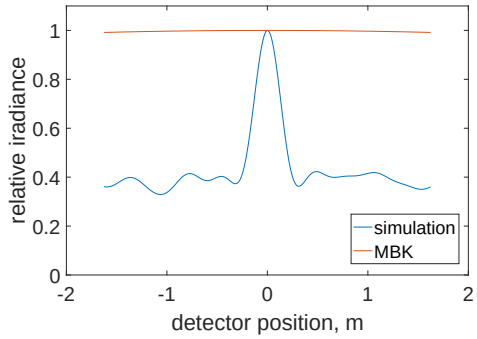

(a) $\lambda = 5\mu m$ is inconsistent with the MBK predictions.

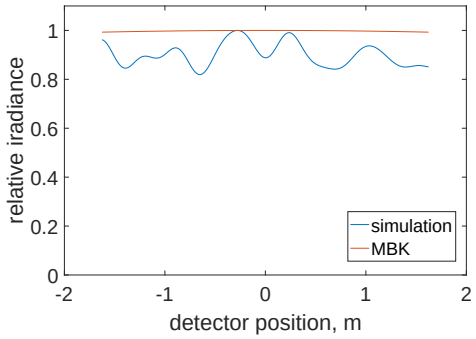

(b) $\lambda = 4\mu m$ is consistent with the MBK predictions.

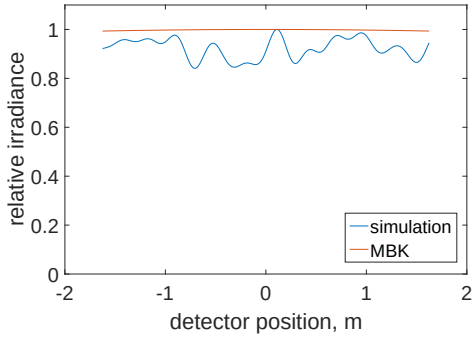

(c) $\lambda = 3\mu m$ is consistent with the MBK predictions.

Figure 4.10. Direct comparison of MBK with the far field scatter of a surface with $\sigma_h = 2.5\mu m$, and $l_{cr} = 100\mu m$, for multiple incident wavelengths.

explanation is posited. It is possible that the response is due to a "global tilt." In this scenario, a single instance the far field is less dominated by speckle, as would be expected for a surface with a longer correlation length. However, the longer correlation length generates a semi-periodic structure across the surface (similar to a grating) causing a slight spatial variation in the location of the maximum for each instance of the rough surface. When this is averaged over many instances, it causes what appears to be a widening of the central lobe.

The simulation is well-suited to comparison with physical optics models, as the simulation is a physical optics simulation. Comparison to microfacet models is a little less straightforward. Several microfacet models were organized into a common form

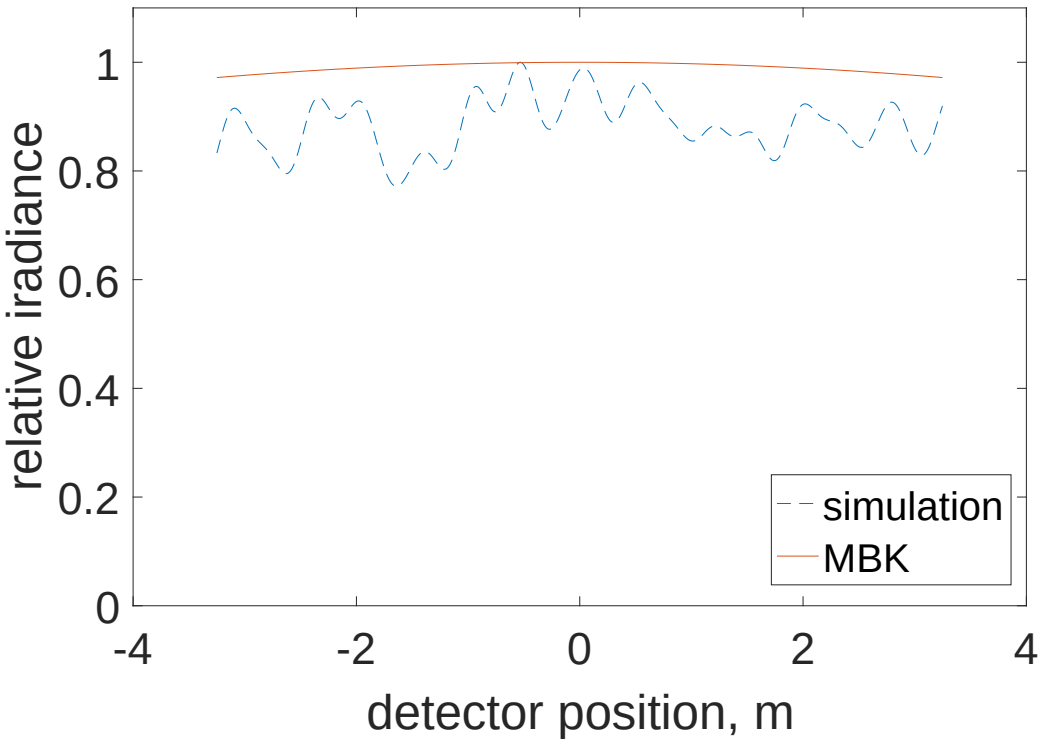

Figure 4.11. Direct comparison of the MBK model with the far field scatter of a surface with $\sigma_h = 2.5\,\mu m$, $l_{cr} = 100\,\mu m$, $\lambda = 3\,\mu m$, and a detector size double previous simulations. It is consistent with the MBK predictions.

by Butler in [5], here the simulation results will be compared to two of the models discussed therein, Cook-Torrance microfacet and Priest microfacet. The two models are quite similar, and were chosen for comparison because they both assume a Gaussian distribution of microfacets. It is worth recalling that the microfacet distribution is not the same as the surface height distribution, but is the distribution of surface slope. Beckmann derived [8] the distribution of surface slopes for Gaussian correlated surfaces. While no empirical result is shown here, as the surface is shown to be Gaussian correlated in Figure 4.1, it is anticipated that the surface slope distribution will be consistent with Beckmann's result.

Microfacet models are heavily parameterized. Cook-Torrance and Priest both have five parameters and therefore run the risk of forcing parameters to achieve a fit,

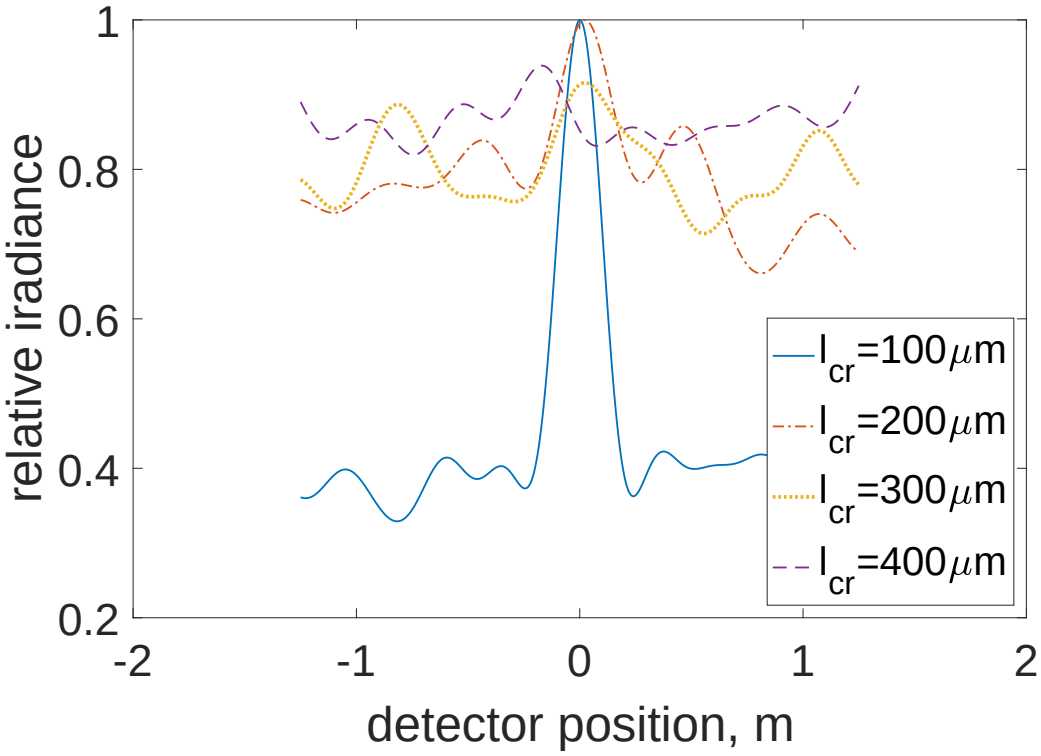

Figure 4.12. Far field irradiance with varying correlation lengths, with $\lambda = 5\mu m$, and $\sigma_h = 2.5\mu m$ shows an anomalous broadening of the far field irradiance pattern with increasing correlation length. The anomaly is credited to a global tilt generated on the surface for longer correlation lengths.

which can result in non-physical parameters. Some attempt was made to keep the parameters physical. Because of the surface roughness regime in the simulation, it was assumed that the diffuse scatter would dominate which in turn forced the overall fit parameters ρ_s and ρ_d. Additionally, as the surface in the simulation was modeled as a perfect conductor, the index of refraction of a "good conductor," in this case silver, was selected. The metric used to define the qualities of a good conductor was zero transmittance for any practical sample width (multiple wavelengths thick). The width of the microfacet distribution was then the only fitting parameter tested heuristically.

While the microfacet model has no explicit dependence on wavelength, microfacet models with a Fresnel term have an implicit dependence on wavelength. The Fresnel

term is a function of surface index of refraction, which is a function of wavelength. In Figures 4.13a and 4.13b microfacet predictions are shown for wavelengths $\lambda = 3\,\mu m$, $\lambda = 4\,\mu m$, and $\lambda = 5\,\mu m$. There is no distinguishable variation for the three wavelengths, but a slight difference between the two models is apparent. This is due largely to the presence of a geometric attenuation, or shadowing and masking, term in the Cook-Torrance model which is not present in the Priest model and may be due to a $\sqrt{2}$ difference in the overall normalization of the microfacet distribution, at least in part.

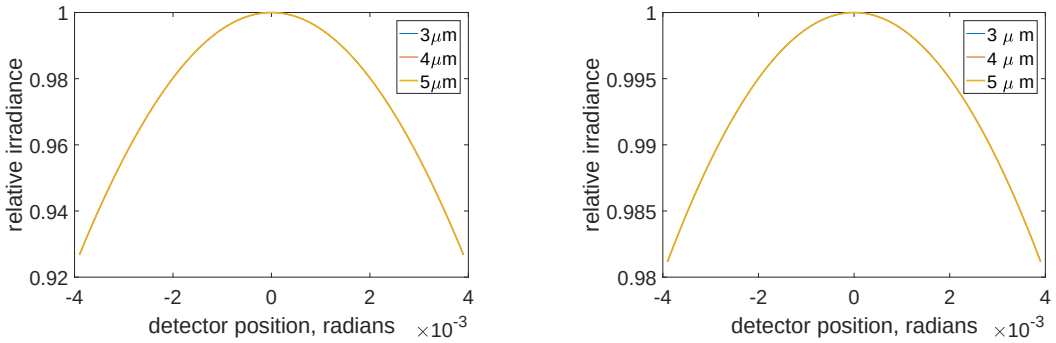

(a) Priest microfacet **(b) Cook-Torrance microfacet**

Figure 4.13. In plane predictions of the far field irradiance from microfacet models show a slight variation across the aperture, no variation between wavelengths, and a slight variation between the two models.

Holding all parameters constant, Figure 4.14 shows comparisons of Priest and Cook-Torrance to the simulation at $\lambda = 3\,\mu m$ and $\lambda = 4\,\mu m$ respectively. The results are consistent, though perhaps the Cook-Torrance is slightly moreso. This may be a result of the geometric attenuation or possibly idiopathic because of the parameters chosen.

Here some discussion of the microfacet distribution is worthwhile. Both Priest microfacet and Cook-Torrance use a Gaussian distribution parameterized by the variable m, with $\sqrt{2}$ variation between them. The Cook-Torrance microfacet distribution is

defined as [5]

$$D_b(\theta_h)\frac{1}{\pi m\cos^4\theta_h}\exp\left[-\left(\frac{\tan\theta_h}{m}\right)^2\right], \tag{4.8}$$

and the Priest microfacet distribution is defined as [5]

$$D_g(\theta_h)\frac{1}{2\pi\sigma_g\cos^4\theta_h}\exp\left[-\left(\frac{\tan\theta_h}{2\sigma_g}\right)^2\right], \tag{4.9}$$

where $\sigma_g = m\sqrt{2}$. Allowing $m = \sigma_g/2 = 2\sigma_s/l_{cr}$ drives the microfacet distribution to be identical to the microfacet distribution given by Beckmann [8]. The fits done in this chapter are near parameterized closely to Beckmann's distribution, with $m = 0.014$ where Beckmann requires the distribution width to be $m = \sigma_h/l_{cr} = 0.025$. When keeping the parameters consistent, those used for $\lambda = 3\,\mu m$ and $\lambda = 4\,\mu m$, the microfacet model predictions are inconsistent with the simulation for $\lambda = 5\,\mu m$ as it was with the MBK model. Comparison of the microfacet models to simulated data with incident light of wavelength $\lambda = 5\mu m$ is shown in Figure 4.15a and 4.15b. However, by drastically changing the microfacet distribution width, a fit may be achieved. Interestingly, the specular and diffuse fitting terms ρ_s, and ρ_d had a negligible effect on the overall shape. Figure 4.16 shows the fit. It is unlikely that this fit is physical, as the microfacet distribution is not a function of wavelength, but is rather an example of spurious parameterization.

The predicted irradiance for the geometry simulated has a small, but distinct, bowing across the observed region. Due to random behavior on the far field irradiance, quadratic fits were done to ascertain whether the data truly exhibited a similar behavior. For the $\lambda = 4\,\mu m$ case, the fit is shown in Figure 4.17a. The fit appears to exhibit a quadratic behavior similar to the predicted irradiance. While the fit may be indicative of an over all bowing behavior, it is possible that the fitting algorithm is fitting to local, rather than global, extrema. Figure 4.17b, the fit for the $\lambda = 3\,\mu m$

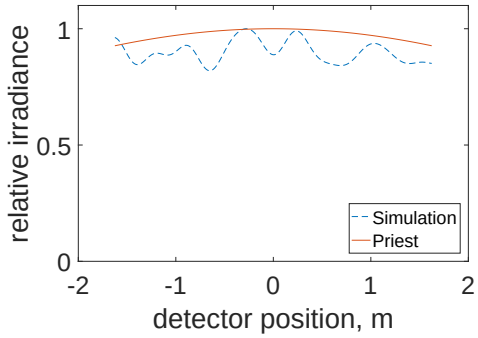

(a) Comparison of Priest to simulated scatter for $\lambda = 4\,\mu m$.

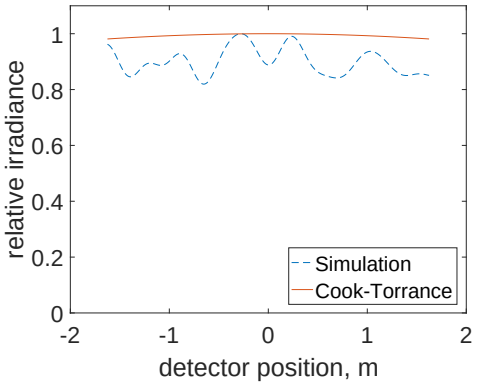

(b) Comparison of Cook-Torrance to simulated scatter for $\lambda = 4\,\mu m$.

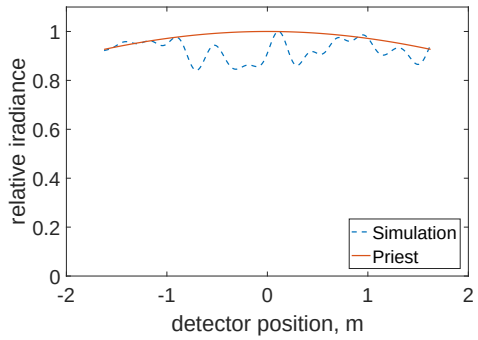

(c) Comparison of Priest to simulated scatter for $\lambda = 3\,\mu m$.

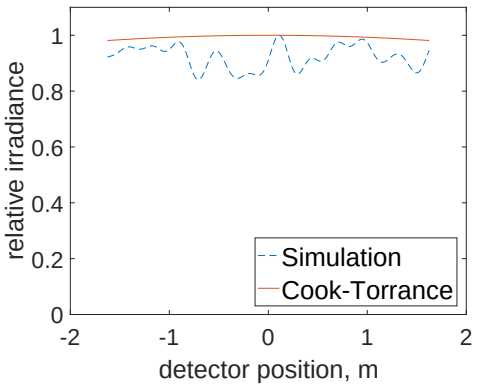

(d) Comparison of Cook-Torrance to simulated scatter for $\lambda = 3\,\mu m$.

Figure 4.14. Comparison of microfacet models to simulated scatter for a surface with $\sigma_h = 2.5\,\mu m$ and $l_{cr} = 100\,\mu m$. With fit parameters of $\rho_s = .1$, $\rho_d = .9$, and $m = \sqrt{2}$ for multiple wavelengths and models.

case, shows a quadratic fit inconsistent with the predicted irradiance, here it appears that the fitting algorithm has captured a local minima.

For completeness, the quadratic fits for the $\lambda = 4\,\mu m$ case are shown alongside the irradiance predictions in Figure 4.18. However, due to concerns about local extrema, the comparison should not be considered a rigorous method of validation.

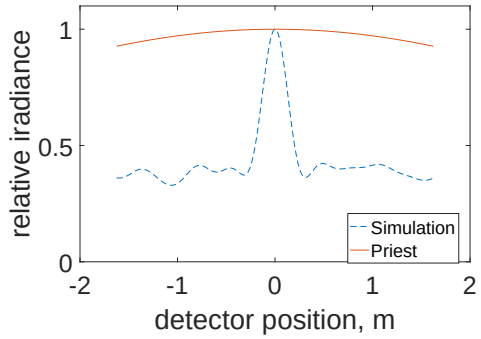

(a) Comparison of Priest to simulated scatter

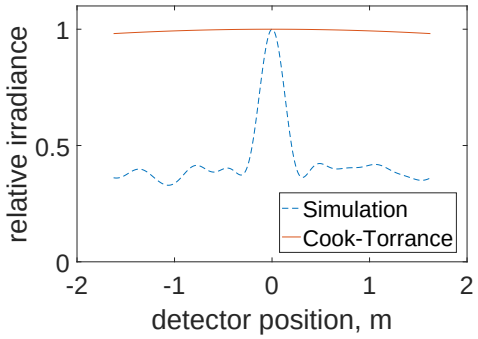

(b) Comparison of Cook-Torrance to simulated scatter

Figure 4.15. Comparison of microfacets models to simulated scatter for $\lambda = 5,\ \mu m$ and a surface with $\sigma_h = 2.5\,\mu m$ and $l_{cr} = 100\,\mu m$. With fit parameters of $\rho_s = .1$, $\rho_d = .9$, and $m = \sqrt{2}$

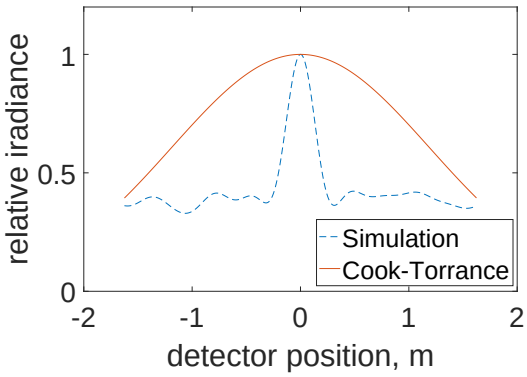

Figure 4.16. Comparison of Cook-Torrance to simulated scatter for $\lambda = 5\mu m$ and a surface with $\sigma_h = 2.5\,\mu m$ and $l_{cr} = 100\,\mu m$. With fit parameters of $\rho_s = .1$, $\rho_d = .9$,

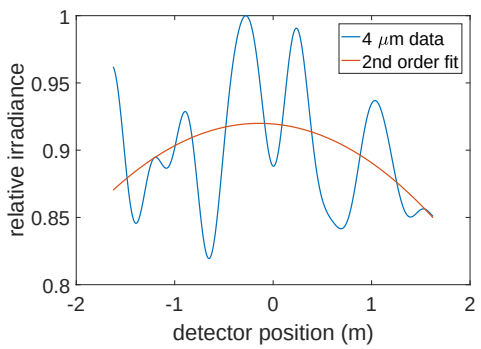

(a) $\lambda = 4\,\mu m$

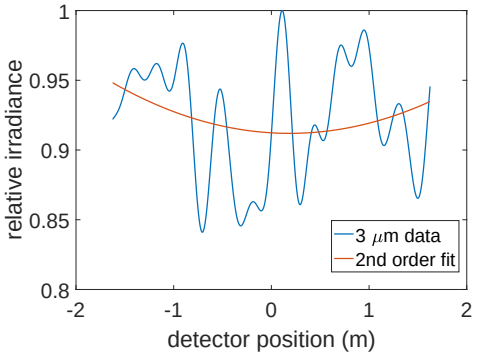

(b) $\lambda = 3\,\mu m$

Figure 4.17. Quadratic fits to simulated data

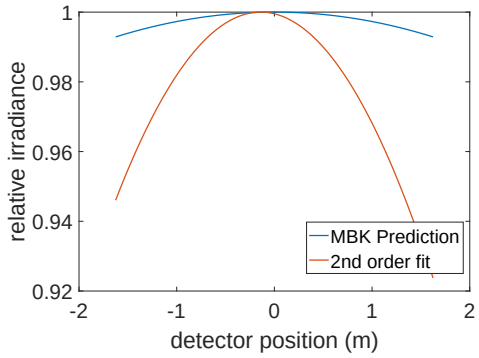

(a) Modified Beckmann Kirchoff

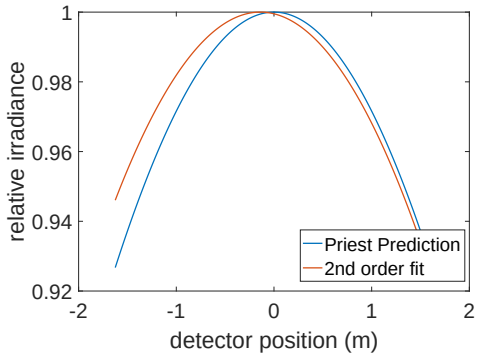

(b) Priest microfacet

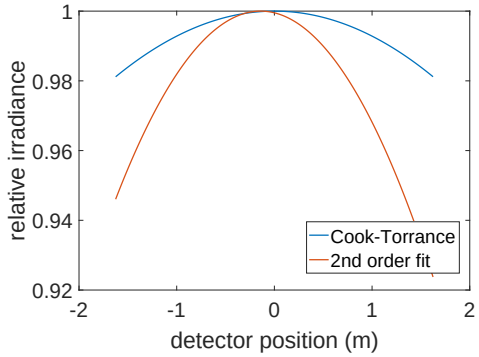

(c) Cook-Torrance Microfacet

Figure 4.18. Quadratic fits to the $\lambda = 4\,\mu m$ is compared to predictions of irradiance for three models

V. Conclusion

The Hyperspectral Remote Sensing community would greatly benefit from BRDF models which have a closed form solution, model wavelength dependence, are computationally efficient, and are valid over a broad range of wavelengths. Though the BRDF community has a rich body of work that is rife with models, none boast all the desired traits. Moreover, verification of existing models over multiple wavelength regimes is made difficult by the need for laser illumination at multiple, close spaced, wavelengths. Additionally, fine control over statistical features of the surfaces under test is difficult to achieve. This thesis sought to develop a wave-optics code that simulates statistically rough surfaces, as well as propagated scatter from those surfaces, for use in verifying BRDF models.

In order to compare rough surface scatter to the Modified Beckmann Kirchoff, Cook-Torrance microfacet, and Priest microfacet models, a Fourier technique for generating turbulence was adapted to generate random rough surfaces with known statistical behavior. In order be consistent with the models chosen for comparison, Gaussian height distributed and correlated surfaces were generated, though the Fourier technique used is suitable for any surface that is well described by a Power Spectral Density. The Gaussian surface was then illuminated with a unit amplitude plane wave and its scatter propagated to the far field. Far field scatter was averaged over a statistically significant number of statistically random surfaces and compared with the aforementioned BRDF models. While verification of both MBK and microfacet models over the entire hemisphere is desirable, computational capability and simulation geometry ultimately restricted evaluation to a small fraction of the total hemisphere.

For sufficiently rough surfaces, all three models were consistent with the far field scatter. However, for surfaces with an RMS surface height, $\sigma_h \lessapprox \lambda/2$, all three models

significantly under-predicted the specular response, which is consistent with previous findings [27]. Ideally, the simulations would be repeated with increased computational power in order to evaluate scatter over a larger fraction of the hemisphere, which is discussed later in this chapter.

The computational tool developed in this thesis provides agility in accessing various wavelengths, surface parameters, and various types of statistically random surfaces. Such an agile simulation provides an avenue for making meaningful comparisons between simulation and models and may be an option for populating BRDF databases in wavelength regimes where data is sparse, such as the long wave infrared.

5.1 Future Work

There are numerous areas of continued investigation on this topic. The work in this thesis realistically represents a baseline study of optical scatter from statistically rough surfaces. This section offers possible topics for continued research.

5.1.1 High Power Computing Simulation Parameterization

Perhaps the most readily apparent next step would be to repeat the work performed in this thesis with greater computational power, more specifically, using a computer with a larger memory capacity. The work in this thesis was performed using 16GB of RAM, which allowed array sizes of 4096x4096 elements to be propagated. Because Fast Fourier Transforms typically require a power of 2 for optimal performance, the next size larger array would be 8192x8192, which 16 GB of RAM could not process repeatedly. Doubling the RAM to 32 GB, or tripling to 64 GB, would likely represent the ability to double and triple the size of the detector in the far field, and therefore, double or triple the angular width that could be examined in the far field. This could open the door to more satisfactory verification of BRDF at

numerous wavelengths and surface profiles. This work would be particularly beneficial in the LWIR, which Butler demonstrated required better BRDF models [3].

High Power Computing (HPC) memory varies between HPC systems, but assuming both a few common memory capacities, and that the HPC is amenable to Object Oriented computing (as is used in WaveProp™) a baseline parameterization of numerical studies can be accomplished.

For this baseline parameterization, it will be assumed that a doubling in memory capacity represents the ability to double the array sizes that can be managed by MATLAB®. RAM availabilities of 64 GB, 128 GB, and 256 GB are considered. The parameters to be varied are detector size and surface correlation. Maintaining all other parameters (e.g wavelength, propagation distance, target size, RMS surface height, etc.), the variations given in Table 5.1 would allow for some interesting investigation. First, nearly $0.06 radians$ of angular spread could be investigated, which fills a substantial portion of the small-angle space for which the simulation is valid. Second, with the ability to appropriately sample shorter correlation lengths (and therefore rougher surfaces), a parametric study of scatter as a function of correlation length could be studied for both physical optics and microfacet models. Additionally, with shorter correlation lengths, the regimes of validity for Beckmann's microfacet distributions from Equations (2.37) and (2.39) could be investigated.

Table 5.1. Specifications for surface correlation and detector size for an HPC computing parameterization

Available RAM	16GB	64GB	128GB	256GB
Detector Size	3.25m	13m	26m	52m
Max Array Size	4096	16384	32768	65536
Surface Array Size	1024	4096	8192	16384
Sample Size	$9.7\,\mu m$	$2.4\,\mu m$	$1.2\,\mu m$	$.61\,\mu m$
Min l_{cr}	$97\,\mu m$	$24\,\mu m$	$12\,\mu m$	$1.2\,\mu m$

5.1.2 Non-planar observation

At some point, additional computational power will no longer ameliorate the far field observation as the detector is flat which restricts observation to small angles. Potentially, a simulation that has a hemispherical detector, or even a half circular in-plane detector could be developed. This would have two principle benefits: the observation results would no longer be restricted to small angles and off-normal incidence and observation would be feasible. Currently, off-normal incidence and observation is restricted both by the overall size of the detector and the fact that the detector is a plane. Off-normal incidence simulations would also be beneficial for comparison to experimental data, as normal incidence and observation cannot be achieved simultaneously in experiment.

5.1.3 Closed form wavelength dependence

A third topic of interest would be to extend this work toward the overarching of this research area: a wavelength dependent closed form BRDF model. Fourier techniques may be used to take the derivative of a surface generating using the techniques developed in this thesis. This information could be used to investigate the surface slope distribution of the surface. Noting that the distribution of interest would be proportional to the derivative of the surface height standard deviation to the correlation length as opposed to the surface height to surface position. In turn,it would be possible to investigate wavelength dependence in a closed form model by calculating the slope distribution in the phase profile rather than the surface profile. Fourier methods could be implemented for these phase screens to derive an overall phase 'microfacet' distribution, which could potentially be used to approximate wavelength dependence into a microfacet-like closed form model.

While Gaussian distributed and correlated surfaces are convenient mathematically,

it is unclear whether they occur frequently in nature. Both linear systems simulations and linear systems analytic solutions for surfaces that exhibit surface statistics other than Gaussian distribution and correlation would be beneficial. For example, using only the numerical tool used in this thesis, a uniformly distributed rough surface or any surface that may be described by a PSD may be readily simulated. While this would not be immediately useful in a field application like HSRS, it could be beneficial to understand more fundamentally the dynamics at play in surface scatter.

Appendix A. Propagation Code

This appendix includes instructions for executing propagation of a rough surface given the code submitted alongside the grading copy of this thesis. As was noted in section 5.1.1, this code was implemented using 16GB of RAM and will not execute otherwise. This code also requires that the user ensure that both the surface generation files and the WaveProp™ Object Oriented Commands are included in the file path.

```
% script_verify_rough_surface
%
clear all; clc;
%
nreals=1;                % number of realizations
plotter = 0;                % plotting flag
Z = 500;                      % range to target [m]
wvl =7e-6;               % wavelength [m]
N = 4096;                     % number of grid points
GBR = 4;                    % gaurd-band ratio
delta = 0.01;               % user-defined parameter
lcr=150e-6;

L_tar = .5e-2               % surface half length [m]
side_tar = 2*L_tar*GBR;     % taget-plane side length [m]
delta_tar = side_tar/N;     % target-plane grid spacing [m]
side_obs = 3             % obs-plane side length [m]
delta_obs =side_obs/N;      % obs-plane grid spacing [m]
[x,y] = meshgrid((-N/2:N/2-1)*delta_obs);
```

```
dx=L_tar/N;
%
P = ...                         % propagation instance
propconvolve(Z,side_tar/side_obs);
T = rectpupil(2*L_tar);         % target instance
%
tau = zeros(N);                 % mutual coherence funtion (MCF)
mu = tau;                       % complex degree of coherence (CDOC)
mask = ...                      % correlation mask
rect(x,side_obs).*rect(y,side_obs);
PIBmask=rect(x,side_obs/4).*rect(y,side_obs/4);
%irr=zeros(N);
irr=zeros(N);
npib=5;
pibreals=1:nreals;
PIB=zeros(1,nreals);
k=2*pi/wvl;
R1=zeros(1023);
sigh=1.6e-6;

for idx = 1 : nreals
idx
%
[s1,s2]=ft_phase_screen_gaus_lanari(lcr,N,delta_tar,sigh); %phase
E_tar = ...                 % target-plane field instance
T(emfield(exp(1i*2*pi/wvl*s1),wvl,side_tar,[],Z,-1,'m','W^{1/2}/m'));
%
%p=phzscreen(s1,side_tar);
```

```
% E_tar = ...              % target-plane field instance
%T(emfield(phz,wvl,side_tar,[],Z,-1,'m','W^{1/2}/m'));


%     if plotter == 1
%         figure(1); clf;
%         colorplt(phase(E_tar));
%         xlabel('y (mm)'); ylabel('x (mm)')
%         title('');
%         %
%         figure(2); clf;
%         colorplt(irradiance(E_tar));
%         xlabel('y (mm)'); ylabel('x (mm)')
%         title('');
%     end
%
E_obs = P(E_tar);         % obs-plane field instance
%
%     if plotter == 1
%         figure(3); clf;
%         colorplt(irradiance(E_obs));
%         xlabel('y (mm)'); ylabel('x (mm)')
%         title('');
%         %
%         figure(4); clf;
%         colorplt(phase(E_obs));
%         xlabel('y (mm)'); ylabel('x (mm)')
%         title('');
```

```
76 %     end
77 %
78 tau = tau + corr2_ft(E_obs.data,E_obs.data,mask,delta_obs);
79 mu = mu + tau/tau(N/2+1,N/2+1);
80 irr=irr+irradiance(E_obs);
81 PIB(1,idx)=sum(sum(PIBmask.*irr))./idx;
82 % PIB(1,idx)=sum(PIBstrip);
83 %phase correlation
84 phz=phase(E_tar);
85 phz=phz.data;
86 R1t=ift2(fftshift(abs(fft2(fftshift(phz(1538:2560,1538:2560))*dx^2)).^2)1/(1024*dx));
87 R1=R1+R1t;
88 %
89 end
90 xobs=-side_obs/2:delta_obs:side_obs/2-delta_obs;
91 % xtar=-.04/2:delta_tar:.04/2-delta_tar;
92 % figure; colorplt(irr./nreals),...
93 %     title(['average observed irradiance at z=',num2str(Z),'m with a ...
    detector size of ',num2str(side_obs),'m'],...
94 %           ['wavlength=',num2str(wvl),', ...
    sigma_h=',num2str(sigh/wvl),'\lambda']),
95
96 figure; plot(xobs,irr.data(N/2+1,:)/nreals),...
97 title({['average observed irradiance at z=',num2str(Z),'m with a ...
    detector size of ',num2str(side_obs),'m'],...
98 ['wavlength=',num2str(wvl),', sigma_h=',num2str(sigh/wvl),'\lambda']}),
99 xlabel('Detector position, m'),ylabel('Irradiance')
100 %  figure; plot(pibreals,PIB);...
```

```
101 %     title(['Average Power in the Bucket over ',num2str(nreals),' ...
        realizations']);
102 % % figure; plot(xtar,R1(ceil(1023/2),:)),...
103 %    title({['correlation of phase for ...
        \sigma_h=',num2str(sigh)],['lambda=',num2str(wvl)]}),
104 % xlabel('aperture position, m'),ylabel('correlation')
105 % figure; histogram(phz),title({['phase distribution resulting from a ...
        gaussian surface with'],['\sigma_h=2.5\mum'],['\lambda=5.6\mum']}),
106 % xlabel('phase, radians'),ylabel('pixels per phase value')
107 % figure; plot(xtar,phz(512,:))
108 % title({['profile of phase screen, ...
        \sigma_h=',num2str(sigh)],['\lambda=',num2str(wvl),' l_{cr}=300\mum']})
109 % xlabel('surface position, m');ylabel('phase, radians')
110 % %
111 % [r,mu_avg] = azimuthal_average(x,y,mu/nreals);
112 % %
113 % figure(5); clf;
114 % plot(r*2*L_tar/(Z*wvl),abs(mu_avg));
115 % xlabel('2Lr/(\lambdaZ)'); ylabel('|\mu|');
116 % line([1 1],[0 1]); axis([0 2 0 1]);
```

A significant portion of the code is commented out, this is to avoid being inundated with plots every time the code is run. This first section sets many of the parameters for the propagation. `nreals` is the number of realizations (ultimately the number of times the far field scatter will be averaged). `plotter` is a binary plotter flag to alert whether the For loop will produce plots. `Z` is the propagation distance. `wvl` is the wavelength of the incident light in meters. `N` is the number of grid points and should be a power of two for the Fourier Transforms. `GBR` is the guard band ratio,

or the ratio of the target to the absorbing boundary. `lcr` is the surface correlation length. `L_tar` is the surface half length. `Side_tar` is the total diffracting aperture size with the guard band. `Delta_tar` is the target sampling. `Side_obs` is the detector side width and is subject to WaveProp™ sampling requirements. `delta_obs` is the detector sampling. `[x,y]` sets up the detector grid used in the far field. Finally, `dx` is a restatement of the target sampling.

```
nreals=1;                % number of realizations
plotter = 0;                 % plotting flag
Z = 500;                      % range to target [m]
wvl =7e-6;               % wavelength [m]
N = 4096;                     % number of grid points
GBR = 4;                     % gaurd-band ratio
delta = 0.01;                % user-defined parameter
lcr=150e-6;

L_tar = .5e-2                % surface half length [m]
side_tar = 2*L_tar*GBR;      % taget-plane side length [m]
delta_tar = side_tar/N;      % target-plane grid spacing [m]
side_obs = 3             % obs-plane side length [m]
delta_obs =side_obs/N;       % obs-plane grid spacing [m]
[x,y] = meshgrid((-N/2:N/2-1)*delta_obs);
dx=L_tar/N;
```

The next section begins setting up the WaveProp™ objects. `P` is an instance of propconvolve which solves the Fresnel Convolution integral for a given target instance, which is define by `T` as our previously surface in a rectangular aperture. `tau`,`mu`,`mask`, `PIBmask`, `irr`, `PIB`,and `R1`preallocate arrays for measurements we may desire. `k` is the

wavenumber of the incident light, and 'sigh' is the RMS surface height of the surface we will generate.

```
%
P = ...                          % propagation instance
propconvolve(Z,side_tar/side_obs);
T = rectpupil(2*L_tar);          % target instance
%
tau = zeros(N);                  % mutual coherence funtion (MCF)
mu = tau;                        % complex degree of coherence (CDOC)
mask = ...                       % correlation mask
rect(x,side_obs).*rect(y,side_obs);
PIBmask=rect(x,side_obs/4).*rect(y,side_obs/4);
irr=zeros(N);
pibreals=1:nreals;
PIB=zeros(1,nreals);
k=2*pi/wvl;
R1=zeros(1023);
sigh=1.6e-6;
```

The `for` loop actually executes the propagation `s1` and `s2` are the random surfaces to be propagated, `E_tar` generates an instance of our target plane we defined above and `E_obs` is an instance of he propagated field. Then commented code allows for generation of plots for both the near and far fields using the data from the objects. It's worth noting that the plot commands vary from the regular Matlab plot commands because the propagation generates an object in Matlab as opposed to just data arrays.`tau` and `mu` are measures of the far field correlation that may be of interest for validation in some scenarios. `irr` keeps a running sum of the far field irradiance, `PIB`

measures a power in the bucket as described in IV. `phz` and `R1` take correlation data of the target phase.

```
for idx = 1 : nreals
idx
%
[s1,s2]=ft_phase_screen_gaus_lanari(lcr,N,delta_tar,sigh); %phase
E_tar = ...               % target-plane field instance
T(emfield(exp(1i*2*pi/wvl*s1),wvl,side_tar,[],Z,-1,'m','W^{1/2}/m'))
%     if plotter == 1
%         figure(1); clf;
%         colorplt(phase(E_tar));
%         xlabel('y (mm)'); ylabel('x (mm)')
%         title('');
%         %
%         figure(2); clf;
%         colorplt(irradiance(E_tar));
%         xlabel('y (mm)'); ylabel('x (mm)')
%         title('');
%     end
%
E_obs = P(E_tar);         % obs-plane field instance
%
%     if plotter == 1
%         figure(3); clf;
%         colorplt(irradiance(E_obs));
%         xlabel('y (mm)'); ylabel('x (mm)')
```

```
%        title('');
%        %
%        figure(4); clf;
%        colorplt(phase(E_obs));
%        xlabel('y (mm)'); ylabel('x (mm)')
%        title('');
%    end
%
tau = tau + corr2_ft(E_obs.data,E_obs.data,mask,delta_obs);
mu = mu + tau/tau(N/2+1,N/2+1);
irr=irr+irradiance(E_obs);
PIB(1,idx)=sum(sum(PIBmask.*irr))./idx;
phz=phase(E_tar);
phz=phz.data;

R1t=ift2(fftshift(abs(fft2(fftshift(phz(1538:2560,1538:2560))*dx^2)).^2),1/(1024*dx));
R1=R1+R1t;
%
endcontent...
```

This generates a 2D color map of the far field irradiance.

```
xobs=-side_obs/2:delta_obs:side_obs/2-delta_obs;
% xtar=-.04/2:delta_tar:.04/2-delta_tar;
% figure; colorplt(irr./nreals),...
%     title(['average observed irradiance at z=',num2str(Z),'m with a ...
    detector size of ',num2str(side_obs),'m'],...
%           ['wavlength=',num2str(wvl),', ...
```

```
    sigma_h=',num2str(sigh/wvl),'\lambda']),
```

This generates the in-plane measurement of far field irradiance

```
figure; plot(xobs,irr.data(N/2+1,:)/nreals),...
title({['average observed irradiance at z=',num2str(Z),'m with a ...
    detector size of ',num2str(side_obs),'m'],...
['wavlength=',num2str(wvl),', sigma_h=',num2str(sigh/wvl),'\lambda']}),
xlabel('Detector position, m'),ylabel('Irradiance')
```

Generates a plot of PIB as function of realizations to verify statistical significance has been achieved.

```
%  figure; plot(pibreals,PIB);...
%     title(['Average Power in the Bucket over ',num2str(nreals),' ...
    realizations']);
```

Plots the phase correlation of the target.

```
% % figure; plot(xtar,R1(ceil(1023/2),:)),...
%    title({['correlation of phase for ...
    \sigma_h=',num2str(sigh)],['lambda=',num2str(wvl)]}),
% xlabel('aperture position, m'),ylabel('correlation')
```

Histograms the phase distribution of the surface.

```
% figure; histogram(phz),title({['phase distribution resulting from a ...
    gaussian surface with'],['\sigma_h=2.5\mum'],['\lambda=5.6\mum']}),
```

```
% xlabel('phase, radians'),ylabel('pixels per phase value')
```

Plots a phase profile of the surface.

```
% figure; plot(xtar,phz(512,:))
% title({['profile of phase screen, ...
    \sigma_h=',num2str(sigh)],['\lambda=',num2str(wvl),' l_{cr}=300\mum']})
% xlabel('surface position, m');ylabel('phase, radians'
```

Appendix B. Code Made Available

Code that was made available with this thesis includes:

- `script_verify_rough_surface_lanari_pib.m` which was outlined previously and generates a rough surface and propagates is scatter,
- WaveProp™packages, which contains the appropriate objects for propagation,
- `ft_phase_screen_gaus_lanari.m` which is a function that may be called to generate surfaces with a Gaussian PDF.

The code was provided on DVD+R alongside the hard copy of this thesis.

Appendix C. GSM Model Beam

The phase is modeled by

$$\phi\left(x,y\right)=r\left(x,y\right)\otimes f\left(x,y\right) \tag{C.1}$$

where $r\left(x,y\right)$ is a delta correlated array of Gaussian distributed random numbers and $f\left(x,y\right)$ is a Gaussian filter. The array, $r(x,y)$, of random numbers has a variance of σ_r^2 and the filter, $f(x,y)$, has a variance of σ_f^2 and is sometimes called the width parameter. The autocorrelation of the amplitude transfer function is

$$R\left(x^{'},y^{'}\right)=\exp\left\{\frac{\sigma_r^2}{2\pi\sigma_f^2}\left[1-\exp\left(-\frac{x\prime^2+y\prime^2}{2\sigma_f^2}\right)\right]\right\}. \tag{C.2}$$

When,

$$\frac{\sigma_r^2}{2\pi\sigma_f^2}>>1. \tag{C.3}$$

and we define the correlation length,

$$l_{cr}^2=\frac{4\pi\sigma_f^4}{\sigma_r^2}, \tag{C.4}$$

results in a Gaussian correlation

$$R\left(x^{'},y^{\prime}\right)\approx\exp\left(-\frac{x\prime^2+y\prime^2}{l_{cr}^2}\right). \tag{C.5}$$

Computationally, this is achieved in the Fourier domain using the property of a linear filter,

$$|\Phi\left(f_x,f_y\right)|^2=\sigma_r^2|F\left(f_x,f_y\right)|^2. \tag{C.6}$$

An $m \times n$ array of zero mean unit variance is generated as $\mathcal{F}\{r(m,n)\}$, and multiplied by the filter,

$$F(f_x, f_y) = \exp\left[-\pi^2 \sigma_f^2 \left(f_x^2 + f_y^2\right)\right], \tag{C.7}$$

and inverse Fourier transformed resulting a unit variance Gaussian correlated array. A best practice is to populate the array with complex numbers, the real and imaginary parts may be inverse Fourier transformed this results in two independent random arrays.

This was implemented in Matlab and the predicted normalized correlation,

$$ACF(x,y) = \exp\left(-\frac{x^2 + y^2}{l_{cr}^2}\right) \tag{C.8}$$

is readily achieved, as shown in Figure C.1. However, this method does not readily provide control of the standard deviation of the Gaussian surface. Reducing the filter width reduces the standard deviation, but once the size of σ_f no longer satisfies Equation (C.3) the correlation length no matches longer theory. Another attempt to achieve the desired standard deviation was to scale the phase screen element wise by the ratio of the desired standard deviation to standard deviation produced. This results in extreme broadening of the correlation.

Additionally, the MBK models of diffracted radiance and BRDF posit no assumptions about the field, but rather about the surface height distribution and correlation. A few attempts were made to choose parameters that would result in reasonable height and correlation lengths for the surface before it became clear that the first approach was not appropriate for controlling the surface.

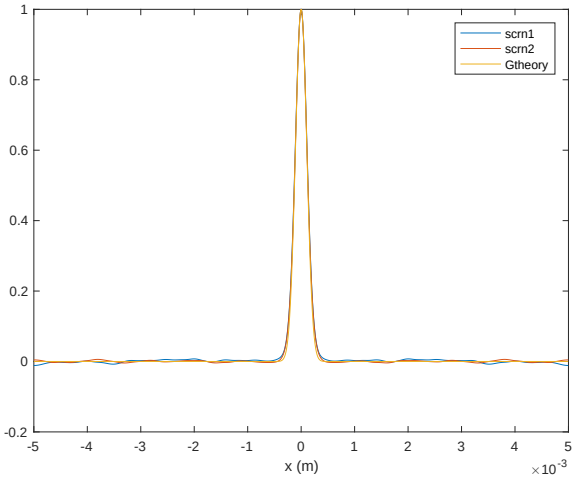

Figure C.1. The surface autocorrelation of two independent surfaces is averaged over 250 instances of the surface. The average autocorrelation is plotted against the theoretical autocorrelation.

Bibliography

[1] M. T. Eismann, *Hyperspectral Remote Sensing.* Bellingham, WA: SPIE Publishing, 2012.

[2] F. Nicodemus *et al.*, "Geometrical consideration and nomenclature for reflectance," *National Bureau of Standards*, 1977.

[3] S. D. Butler, "Experimental and theoretical basis for a closed-form spectral BRDF model," Ph.D. dissertation, Air Force Institute of Technology, Wright Patterson AFB, Ohio, 2015.

[4] J. Jackson, *Classical Electrodynamics*, 3rd ed. Hoboken, NJ: J. Wiley and Sons, 1999.

[5] S. Butler and M. Marciniak, "Robust categorization of microfacet BRDF models to enable flexible application-specific BRDF adaptation," *Proceedings of the SPIE*, vol. 9205, 2014.

[6] S. Rusinkiewicz, "A new change of variable for efficient BRDF representation," *Rendering Techniques*, 1998.

[7] R. Cook and K. Torrance, "A reflectance model for computer graphics," *ACM Transactions on Graphics*, vol. 1, pp. 7–24, 1982.

[8] P. Beckmann and A. Spizzichino, *The Scattering of Electromagnetic Waves From Rough Surfaces.* Norwood, MA: Artech House Inc, 1963.

[9] R. Priest and T. Germer, "Polarimetric BRDF in the microfacet model: Theory and measurements," *proc. 2000 Meeting of the MSS Specialty Sensors Groups on Passive Sensors*, vol. 1, pp. 169–182, 200.

[10] R. Priest and S. Meier, "Polarimetric microfacet scattering theory with applications to absorptive and reflective surfaces," *Optical Engineering*, vol. 41, pp. 988–993, 2002.

[11] B. Sandford and L. Robertson, "Infrared reflectance properties of aircraft paint," *Proc. IRIS Targets, Backgrounds, and Discrimination*, 1985.

[12] B. Phong, "Illumination for computer generated pictures," *Communications of the ACM*, no. 18, 1975.

[13] S. E. Freda, "Microfacet wavelength-scaling of the BRDF," Master's thesis, Air Force Institute of Technology, Wright Patterson AFB, Ohio, 2016.

[14] A. Krywonos, "Predicting surface scatter using a linear systems formulation of non-paraxial scalar diffraction theory," Ph.D. dissertation, University of Central Florida, Orlando, Florida, 2006.

[15] J. C. Stover, *Optical Scattering: Measurement and Analysis*, 3rd ed. Bellingham, WA: SPIE Pressl, 2012.

[16] J. A. Ogilvy, *Theory of Wave Scattering From Random Rough Surfaces*. Bristol, England: IOP Publishing LTD, 1991.

[17] J. W. Goodman, *Speckle Phenomena In Optics*. Englewood, CO: Roberts and Company, 2007.

[18] J. Harvey, "Light scattering characteristics of optical surfaces," Ph.D. dissertation, University of Arizona, Tucson, Arizona, 1976.

[19] J. Harvey *et al.*, "Nonparaxial scalar treatment of sinusoidal phase gratings," *Journal of the Optical Society of America A*, vol. 23, pp. 858–865, 2006.

[20] J. W. Goodman, *Fourier Optics*, 3rd ed. Englewood, CO: Roberts and Company, 2005.

[21] D. Voelz, *Computational Fourier Optics: A Matlab Tutorial.* Bellingham, WA: SPIE Press, 2011.

[22] J. Schmidt, *Numerical Simulation of Optical Wave Propagation.* Bellingham, WA: SPIE Press, 2010.

[23] E. Wolf, *Introduction to the Theory of Coherence and Polarization of Light.* Cambridge, UK: Cambridge University Press, 2007.

[24] *WaveProp A Wave Optics Simulation System For Use with Matlab*, the Optical Sciences Company, 2010.

[25] E. Dereniak and G. Boreman, *Infrared Detectors and Systems.* Hoboken, NJ: John Wiley and Sons, 1996.

[26] F. Gori, "Far-zone approximation for partially coherent sources," *Optics Letters*, vol. 30, pp. 2840–2842, 2005.

[27] M. F. Spencer, "The scattering of partially coherence electromagnetic beam illumination for statistically rough surfaces," Ph.D. dissertation, Air Force Institute of Technology, Wright Patterson AFB, Ohio, 2015.

Acronym List

- AFIT- Air Force Institute of Technology
- BK- Beckmann Kirchhoff
- BRDF- Bidirectional Reflectance Distribution Function
- CASI- Complete Angular Scatter Instrument
- E- Irradiance
- GSM- Gaussian Schell Model
- HPC- High Performance Computing
- HSRS- Hyperspectral Remote Sensing
- I- Intensity
- L- Radiance
- LWIR- Long Wave Infrared
- MBK- Modified Beckmann Kirchhoff
- MKS- Meters, Kilogram, Seconds
- MWIR- Mid Wave Infrared
- PSD- Power Spectral Density
- RMS- Root Mean Square
- SLM- Spatial Light Modulator
- SMS- Schmitt Measurement Systems

- VNIR/SWIR Visible, Near Infrared/Shortwave Infrared
- WFE- Wave Front Error

REPORT DOCUMENTATION PAGE

Form Approved
OMB No. 0704–0188

1. REPORT DATE *(DD–MM–YYYY)*	2. REPORT TYPE	3. DATES COVERED *(From — To)*
23 Mar 2017	Master's Thesis	Sept 2015 — 23 Mar 2017

4. TITLE AND SUBTITLE

Numerical Wave Optics Investigation of Optical Scatter From Statistically Rough Surface

5a. CONTRACT NUMBER

5b. GRANT NUMBER

5c. PROGRAM ELEMENT NUMBER

6. AUTHOR(S)

Lanari, Ann, M., Captain

5d. PROJECT NUMBER

5e. TASK NUMBER

5f. WORK UNIT NUMBER

7. PERFORMING ORGANIZATION NAME(S) AND ADDRESS(ES)

Air Force Institute of Technology
Graduate School of Engineering and Management (AFIT/EN)
2950 Hobson Way
WPAFB OH 45433-7765

8. PERFORMING ORGANIZATION REPORT NUMBER

AFIT-ENP-MS-17-M-099

9. SPONSORING / MONITORING AGENCY NAME(S) AND ADDRESS(ES)

AFOSR
Att: Dr. Arje Nachman
875 North Randolph St
Ste 325, Room 3112
Arlington VA 22203
Email: arje.nachman@us.af.mil

10. SPONSOR/MONITOR'S ACRONYM(S)

AFOSR

11. SPONSOR/MONITOR'S REPORT NUMBER(S)

12. DISTRIBUTION / AVAILABILITY STATEMENT

DISTRIBUTION STATEMENT A:
APPROVED FOR PUBLIC RELEASE; DISTRIBUTION UNLIMITED.

13. SUPPLEMENTARY NOTES

14. ABSTRACT

The Bidirectional Reflectance Distribution Function (BRDF) describes optical scatter from rough surfaces. Numerical methods can control incident wavelength and surface features. Utilizing Fourier techniques for propagation to the far field, scatter resulting from Gaussian distributed and correlated surfaces is compared to predictions of physical optics and microfacet BRDF models. For RMS surface heights greater than /2, physical optics models are shown to be consistent with resulting scatter for incident light of wavelength $3\,\mu m$ to $5\,\mu m$ and scattered angles of $-2\,\mu rad$ to $2\,\mu rad$ illuminated at normal incidence, while microfacet models fail to predict scatter width for shorter wavelengths

15. SUBJECT TERMS

16. SECURITY CLASSIFICATION OF:			17. LIMITATION OF ABSTRACT	18. NUMBER OF PAGES	19a. NAME OF RESPONSIBLE PERSON
a. REPORT	b. ABSTRACT	c. THIS PAGE			Maj S Butler, AFIT/ENP
U	U	U	UU	94	19b. TELEPHONE NUMBER *(include area code)* (937) 255-3636, x4385; samuel.butler@afit.edu